Tornadogenesis in a Simulated Mesovortex within a Mesoscale Convective System

Alexander D. Schenkman, Ming Xue, and Alan Shapiro

Center for Analysis and Prediction of Storms and School of Meteorology
University of Oklahoma, Norman Oklahoma 73072

February 2012
Submitted to Journal of the Atmospheric Sciences

Corresponding author address:
Ming Xue
Center for Analysis and Prediction of Storms
University of Oklahoma,
120 David L. Boren Blvd, Norman OK 73072
mxue@ou.edu

Abstract

The ARPS model is used to simulate a tornadic mesovortex with the aim of understanding the associated tornadogenesis processes. The mesovortex was one of two tornadic mesovortices spawned by a mesoscale convective system (MCS) that traversed southwest and central Oklahoma on 8-9 May 2007. The simulation used 100-m horizontal grid spacing, and is nested within two outer grids with 400-m and 2-km grid spacing, respectively. Both outer grids assimilate radar, upper air, and surface observations via 5-min 3DVAR assimilation cycles. The 100-m grid is initialized from a 40-min forecast on the 400 m grid.

Results from the 100-m simulation provide a detailed picture of the development of a mesovortex that produces a sub-mesovortex-scale tornado-like vortex (TLV). Closer examination of the genesis of the TLV suggests that a strong low-level updraft is critical in converging and amplifying vertical vorticity associated with the mesovortex. Vertical cross-sections and backward trajectory analyses from this low-level updraft reveal that the updraft is the upward branch of a strong rotor that forms just northwest of the simulated TLV. The horizontal vorticity in this rotor originates in the near surface inflow and is caused by surface friction. An additional simulation with surface friction turned off does not produce a rotor, strong low-level updraft, or TLV. Comparison with previous two-dimensional numerical studies of rotors in the lee of mountains shows striking similarities to the rotor formation presented herein.

The findings of this study are summarized in a four-stage conceptual model for tornadogenesis in this case that describes the evolution of the event from mesovortexgenesis through rotor development and finally TLV genesis and intensification.

1. Introduction

The tendency of quasi-linear convective systems (QLCSs) to produce tornadoes has been well documented (e.g, Forbes and Wakimoto 1983; Przybylinski 1995; Atkins et al. 2004; Davis et al. 2004; Wakimoto et al. 2006a; Atkins and Laurent 2009a, b). Moreover, a climatological study by Trapp et al. (2005) showed that about 18% of tornadoes were spawned by QLCSs. QLCS tornadoes typically form in association with strong, long-lived low-level meso-γ-scale (e.g., Orlanski 1975) vortices, hereafter referred to as mesovortices. These mesovortices are not only associated with tornadoes in QLCSs, but also have been shown to be responsible for most of the wind damage reports associated with QLCSs (e.g., Wakimoto et al. 2006b). Observational studies (e.g., Atkins et al. 2004; Atkins et al. 2005) have found a clear relationship between mesovortex lifetime, strength, and propensity to produce tornadoes. For example, Atkins et al. (2004) find an average lifetime of 76 min for tornadic mesovortices vs. 32 min for non-tornadic mesovortices.

The formation and evolution of mesovortices has been studied in detail through both idealized numerical simulations (Trapp and Weisman 2003; Weisman and Trapp 2003; Atkins and Laurent 2009b, a) and dual-Doppler analyses (e.g., Wakimoto et al. 2006a). Trapp and Weisman (2003) proposed that mesovortices are generated as vortex couplets via downward tilting of southward pointing cold pool vortex lines along the gust front by a precipitation-induced downdraft. However, the dual-Doppler analysis of Wakimoto et al. (2006a) suggested that this downdraft was induced mechanically by the pressure-field rather than by precipitation loading.

Regardless of the origin of the downdraft, the formation mechanism of Trapp and Weisman (2003) and Wakimoto et al. (2006a) implies the anticyclonic vortex is north of the cyclonic vortex in the couplet. In contrast, Atkins and St. Laurent (2009b, hereafter AL09) explain that upward tilting of crosswise southward-pointing cold pool vortex lines occurs due to a locally enhanced updraft along a bulge in the convective outflow[1]. For a low-level westerly momentum surge in the Northern Hemisphere, this implies the cyclonic vortex is the poleward one within the vortex couplet. AL09 also proposes a second mesovortex generation mechanism that involves the development of only a cyclonic mesovortex via tilting of baroclinically generated streamwise horizontal vorticity into the vertical and subsequent stretching by the updraft along the convective storm-generated gust front. The authors note that this genesis mechanism is similar to the proposed mechanism for the genesis of the low-level mesocyclones in supercells (e.g., Rotunno and Klemp 1985). Observational examples exist for vortex couplets due to upward tilting (e.g., Atkins et al. 2004; Atkins et al. 2005)(Wheatley et al. 2006) and downward tilting (e.g., Wakimoto et al. 2006a; Wheatley and Trapp 2008). There is currently little explanation or reconciliation between the differing vortex formation mechanisms of Trapp and Weisman (2003), Wakimoto et al (2006a), and AL09.

While the above studies disagree on the details of the mesovortex formation mechanism and the orientation of the vortex couplet, they do agree that mesovortices tend to be stronger and longer-lived in environments with stronger low-level shear. The studies explain that stronger

[1] This mechanism is similar to the process by which line-end vortices in MCSs develop (Weisman and Davis 1998) as well as to the vortex line arches presented in Straka et al. (2007) and Markowski et al. (2008) by which low-level rotation develops in supercells.

shear leads to updrafts that are stronger and more upright, leading to more intense stretching of low-level vorticity. This result has recently been confirmed in a study by Schenkman et al. (2011a ; hereafter, S11a), wherein real-data experiments that more effectively analyzed low-level shear forecasted stronger, longer-lived mesovortices.

The dynamical link between mesovortices and tornadoes remains relatively unexplored. To the authors' knowledge, no study has examined a case with sufficient resolution (either observationally or numerically) to capture concurrent mesovortex and tornado circulations. The present study aims to do this by analyzing high-resolution numerical modeling results of a real-data initialized convective storm and the associated mesovortex which produced a sub-mesovortex scale tornado-like vortex[2] (hereafter, TLV). An overview of the 8-9 May 2007 mesoscale convective system (MCS) and the associated mesovortices along with an outline for the rest of the paper is presented in the next section.

2. Overview of the 8-9 May 2007 MCS and associated mesovortices

On 8-9 May 2007, an MCS (Fig. 1) moved through much of the western half of Texas and Oklahoma. A well-defined line-end vortex (LEV) developed in the northern portion of the main convective line of the MCS as it moved into southwest Oklahoma. Convective cells associated with the LEV produced several weak tornadoes that struck parts of southwest and central Oklahoma. According to a National Weather Service (NWS) damage survey, the first

[2]We refer to the vortex as 'tornado-like' because even with 100-m grid-spacing, the simulation cannot fully resolve the vortex structure, thus we cannot say for certain that the simulated vortex qualifies as a tornado.

tornado caused EF-1 damage in Grady County, near Minco. Another weak tornado produced EF-0 damage near Union City in Canadian County. The most destructive tornado, a high-end EF-1, caused an estimated three million dollars of damage in El Reno, Oklahoma. Two very short-lived EF-1 tornadoes were reported a short time after the El Reno tornado near Piedmont.

Examination of radial velocity observations of the 9 May 2007 MCS and LEV from the Oklahoma City Terminal Doppler Weather Radar (TDWR) over the period 0300 through 0500 UTC reveals at least five distinct mesovortices (not shown). All of the mesovortices developed on the southeast side of the LEV during the comma-echo stage of the MCS (Fujita 1978). Radar reflectivity observations indicate that the mesovortices were associated with strong convective cells embedded within the head of the comma echo (see the zoomed in portion of Fig. 1). The wind field around the LEV caused the mesovortices to move to the north and west. As the mesovortices intensified, the associated convective cells briefly took on supercellular characteristics with hook-echoes becoming apparent. A particularly well-defined hook echo is apparent in TDWR observations (not shown) of the convective cell associated with the mesovortex that spawned the Minco tornado (hereafter, the Minco mesovortex).

Only two of the five mesovortices present in the 9 May 2007 MCS were tornadic. These two were stronger and longer-lived than the non-tornadic mesovortices (See Table 1 in S11a). Both the Minco and Union City tornadoes appear to have formed in association with the Minco mesovortex. The mesovortex associated with the El Reno tornado formed immediately after the dissipation of the Union City tornado. The El Reno mesovortex persisted after the dissipation of the El Reno tornado and spawned the two brief Piedmont tornadoes (See Fig. 1 for a map with town names).

Numerical forecasts presented in S11a successfully simulated the genesis and evolution of the Minco mesovortex on a 400 m resolution grid. Experiments that assimilated radial velocity data from the CASA IP-I radar network (McLaughlin et al. 2009) were particularly accurate in their forecast of the Minco mesovortex (S11a). In this paper, a simulation with 100-m grid spacing is nested within one of the experiments that assimilated CASA radial velocity (Vr) data (experiment CASAVrZ5MM in S11a), and the model integration is performed only over the lifespan of the Minco mesovortex. We focus on analyzing the results of this high-resolution simulation, and seek to understand and explain the development of the TLV associated with the Minco mesovortex. The rest of this paper is organized as follows: section 3 briefly describes the configurations of the numerical simulations; section 4 describes the evolution of the simulated Minco mesovortex with a detailed analysis of the genesis of a simulated intense low-level TLV. A summary and conclusions are given in section 5.

3. Experiment setup

The numerical simulation was performed using the Advanced Regional Prediction System (ARPS;Xue et al. 1995; Xue et al. 2000; Xue et al. 2001; Xue et al. 2003) model. The ARPS model is three-dimensional, fully-compressible, and non-hydrostatic. It was configured with fourth-order advection in the horizontal and vertical, a rigid top boundary condition with a wave absorbing layer beginning at 12 km AGL,, fourth-order computational mixing, a 1.5-order TKE-based subgrid-scale turbulent mixing scheme and PBL parameterization, and Lin et al. (1983) three-ice microphysics with the rain intercept parameter set to 8.0 x 10^5 m^{-4} according to Snook and Xue (2008). The Coriolis parameter is latitude dependent and includes the effect of earth curvature. A multilayer land surface model is used that is similar to the NOAH land surface model (Chen and Dudhia 2001), with five vertical soil levels. Surface fluxes are determined using a drag coefficient of $3x10^{-3}$, and the skin temperature and top soil moisture content predicted from the land surface model [option *sfcphy*=3, see Xue et al. (1995) for more details]. The domain combines 100-m grid spacing in the horizontal with a vertically stretched grid based on a hyperbolic tangent function (Xue et al. 1995) with a minimum spacing of 20 m near the ground. The model domain is 50 km x 60 km x 30 km with 60 vertical levels.

The 100-m resolution model domain is one-way nested within two outer grids (see Fig. 1). The outermost grid has 2-km horizontal spacing and is intended to capture the overall evolution of the MCS and LEV of 8-9 May 2007 (Schenkman et al. 2011b). A 400-m resolution grid was nested inside of the 2-km grid. This nest was designed to capture the mesovortices associated with the 8-9 May 2007 MCS case, through the assimilation of high-resolution wind data from the CASA radars. Results showed that when the low-level shear in advance of the surface cold pool produced by the MCS was properly analyzed, it was possible to forecast the evolution of the Minco mesovortex with good accuracy. In contrast, simulations with less accurate analyses of the low-level shear produced only weak, short-lived mesovortices. More details on the role of low-level shear in accurately forecasting this event are provided in S11a. A 40-min forecast on the 400-m resolution grid from the CASAVrZ5MM experiment in S11a provided the initial condition at 0300 UTC (through spatial interpolation) and boundary conditions at 5-min intervals to the 100-m resolution grid. As explained in S11a, the CASAVrZ5MM experiment is run with an 80-min assimilation window (0100-0220 UTC) in which observations from WSR-88D, CASA, and Oklahoma Mesonet are assimilated every 5 min. A free forecast is then run from 0220 UTC thru 0500 UTC 9 May 2007. Simulations on the 100-m resolution grid are run from 0300 to 0410 UTC 9 May 2007. The start time of the 100-m simulation (0300 UTC) is slightly before the genesis of the Minco mesovortex in the 400-m simulation. This allows for the detailed examination of both the genesis and intensification of the Minco mesovortex using 100-m grid spacing.

4. The simulated mesovortex and associated tornado-like vortex

a. General overview of the 100-m grid-spacing numerical simulation

The 100-m simulation begins at 0300 UTC with a well-defined gust front at the low levels (Fig. 2a). This gust front marks the leading edge of an outflow surge associated with strong convection near the center of the LEV (see the discussion of the secondary outflow surge in S11a). The gust front is initially oriented north-south. An initial mesovortex[3] is present along the northern portion of the gust front (Fig. 2a). Over the next five minutes, a gust front bulge develops to the southeast of the initial mesovortex. An enhanced updraft develops along the gust front bulge, leading to the generation of cyclonic (anticyclonic) vorticity on the northern (southern) side of the bulge (Fig. 2b). The vortex line plotted in Fig. 2b arches from the cyclonic vorticity to the area of anti-cyclonic vorticity indicating that the baroclinically generated southward-pointing horizontal vortex lines at the gust front are tilted into the vertical at the

---

[3] As in S11a, a circulation is considered a mesovortex if it has maximum vertical vorticity > 0.025 s^{-1} and persists for at least 15 min. These criteria are kept the same despite increased resolution of the present study because mesovortices were already resolved fairly well on the 400 m grid in S11a. Calculations of the Okubo-Weiss number (e.g., Markowski et al. 2011) were also examined (not shown) to verify that mesovortices were in fact vortices and not just long-lived shear lines.

bulge, creating the vorticity couplets. The arrangement of the vorticity centers within the couplets is similar to that of the mesovortex couplets discussed in AL09, because the couplets are generated through enhanced updraft between the vorticity centers.

The initial mesovortex decays rapidly, dissipating by 0315 UTC. S11a also discussed this initial mesovortex and showed that it was short-lived because it was generated in an area of weak low-level shear. Meanwhile, the anticyclonic vorticity on the south side of the gust front bulge remains disorganized and does not form a well-defined anticyclonic mesovortex. In contrast, the cyclonic vorticity on the north side of the gust front bulge intensifies[4] and the Minco mesovortex develops by 0315 UTC (Fig. 2c). S11a found that the Minco mesovortex developed in an area of much stronger low-level shear than the initial mesovortex (see their Fig. 9).

The Minco mesovortex continues to intensify through 0330 UTC. Concurrently, the flow field associated with the mesovortex begins to resemble that of a divided supercell low-level mesocyclone (Lemon and Doswell 1979), with a strong updraft in the western and northern parts of the circulation and a strong downdraft in the eastern sector of the circulation (Fig. 3a). Unlike a supercell, however, there is not a persistent mid-level mesocyclone associated with the

[4] The idealized simulations in Trapp and Weisman (2003) found that the cyclonic circulation in a mesocyclone couplet is favored due to Coriolis forcing. However, the Coriolis force is not important on spatial scales of a few kilometers and temporal scales of a few minutes. As such, in the case under consideration, the pre-existing mesoscale cyclonic vorticity associated with the LEV can also act to enhance the cyclonic circulation, especially through low-level convergence and vertical stretching associated with the cyclonic mesovortex. A similar process will act to weaken the anticyclonic vorticity.

low-level circulation (not shown). A TLV forms in association with the intensifying mesovortex around 0327 UTC. This TLV will be discussed in detail in the next sub-section.

After 0330 UTC, the Minco mesovortex begins to broaden and weaken. As this occurs, the updraft in the western and northern sectors of the mesovortex rapidly weakens, and much of the circulation becomes embedded in downdraft by 0340 UTC (Fig. 3b). By 0355 UTC, the Minco mesovortex broadens substantially with a disorganized vertical velocity field (not shown). The Minco mesovortex gradually decays throughout the remainder of the simulation.

b. Genesis of a tornado-like vortex

Closer examination of the simulated Minco mesovortex reveals the presence of several submesovortex-scale vortices. Most of these vortices are short-lived and do not produce tornado strength winds. However, one of the vortices is longer-lived and produces EF-0 (40 m s^{-1}) strength winds. The remainder of this sub-section discusses this tornado-like vortex (TLV). In this study, we define a TLV as a clearly-discernible area of rotation that persists for at least 2 min with maximum vertical vorticity > 0.2 s^{-1} and winds speeds of EF-0 intensity or greater. For convenience in our discussion of the TLV, the following naming convention is used: the bulging portion of the gust front that extends from the Minco mesovortex to the east is hereafter referred to as the rear-flank gust front (RFGF); the gust front that is located to the west of the Minco mesovortex is referred to as the forward flank gust front (FFGF). This naming convention was chosen because the features closely resemble RFGF and FFGF appearance in supercell storms (e.g., see the schematic in Lemon and Doswell 1979). This naming convention is meant to simplify the description of the TLV-relative location and appearance of these features and *not* to suggest that we are simulating a classic supercell. The FFGF and RFGF are denoted in Fig. 4a.

With the above definitions in mind, the evolution of the TLV is now discussed. The TLV forms very rapidly around 0327 UTC as low-level vorticity associated with the Minco mesovortex[5] along the occluding RFGF moves to the northwest and merges with a small vertical vorticity maximum (while this feature is fairly weak, it is persistent and can be tracked back for several minutes prior to TLV genesis. The role of this feature is discussed at the end of this subsection.) that is associated with a surge of westerly momentum at low levels (Fig. 4a-c). The developing TLV rapidly contracts with maximum vertical vorticity values increasing from 0.1 s^{-1} to 0.4 s^{-1} in about 60 s (Fig. 4d-e). The TLV broadens slightly over the next few minutes while maintaining its intensity (Fig. 5a,b). Around 0333 UTC, the TLV broadens and weakens rapidly (Fig. 5c) as a strong downdraft forms in its eastern half. This downdraft is only present at low-levels and is dynamically induced by the ~12 hPa low-level pressure drop associated with the TLV (Fig. 5a). At the same time, a strong vorticity maximum (marked by 'Y' in Fig. 5c) forms to the west of the TLV center. This vorticity maximum is very short lived and has dissipated by 0335 UTC (Fig. 5d).

While the dynamics behind the mature and decaying stages of the TLV are easily explained by the associated low-level pressure perturbation, the rapid genesis and intensification of the TLV warrant closer inspection. Time-height plots of maximum vertical velocity and

[5] Due to insufficient model resolution and complicated flow evolution, it is very difficult to determine whether the Minco mesovortex simply contracts and becomes the TLV or if some of the vorticity associated with the Minco mesovortex is concentrated with the Minco mesovortex remaining a separate feature. It may also be unlikely that such a distinction is clear in the actual atmosphere.

vorticity indicate that the TLV was associated with a strong updraft, with w > 20 m s^{-1} at 500 m AGL (Fig. 6). This low-level updraft formed before, and dissipated after, the TLV. Backward trajectory calculations terminating in the TLV confirm that this updraft played a key role in TLV intensification as low-level stretching, due to the rapidly increasing updraft above the ground, is the dominant vorticity generation term (Fig. 7). Thus, it is important to determine the mechanism by which this intense low-level updraft was generated and maintained, as it plays a critical role in the TLV genesis and maintenance.

Examination of low-level flow fields in the five minutes leading up to the development of the TLV reveals that the intense low-level updraft forms along the FFGF. The intense low-level updraft is forced by strong near-surface convergence between easterly flow associated with the occluding RFGF and a narrow band of enhanced westerly flow just to the west of the FFGF (Fig. 8a). Vertical cross sections reveal that this westerly flow comprises the bottom part of a rotor that has formed immediately to the west of the FFGF (Fig. 8b). This rotor is about 1 km deep, 2 km wide and 4 km long and is oriented along the FFGF (Fig. 8c). A 600-m diameter ring of 18 backward trajectories that is initialized around the TLV is also plotted in Fig. 8c. The majority of these trajectories pass through the rotor.

The rotor forms around 0320 UTC in association with a surge of westerly momentum at low-levels, which is the result of a low-level downdraft that is associated with the dissipation of the first mesovortex (cf. Fig. 2c). As this surge of momentum impinges on the FFGF from the rear, the rotor circulation rapidly intensifies (this rapid intensification will be discussed and shown further in section 4d.). This rapid intensification is coincident with a ~8 hPa pressure drop [likely due to the increase in horizontal vorticity as reflected in the 'spin' term of the diagnostic pressure perturbation equation (e.g., eq. (2.131) in Markowski and Richardson 2010)], along the central axis of the rotor by 0325 UTC. It is at this point that the strong low-level updraft forms in the ascending branch of the rotor. TLV genesis occurs rapidly as low-level vertical vorticity associated with the Minco mesovortex moves into the strong convergence associated with the low-level updraft/rotor. This can be seen in Fig. 4 as the broad area of vorticity associated with the Minco mesovortex on the left side of the RFGF moves towards FFGF during occlusion.

Another source of vorticity for the TLV is the horizontal vorticity of the rotor itself. Fig. 9 indicates that this vorticity is tilted into the vertical and is responsible for the generation of the small vorticity maximum introduced above and highlighted in Fig. 4a-d. However, a circulation analysis, in which a 200-m radius ring made up of 3600 parcels surrounding the TLV is initialized 100-m AGL and the parcel trajectories are integrated backward in time, indicates that this is likely a secondary effect. More specifically, the circulation around the circuit remains nearly constant while the area it encloses decreases dramatically (Fig. 10). Thus, according to Stoke's theorem, the vorticity component normal to the area enclosed by the circuit must increase. Moreover, most of the circuit during this time is nearly horizontal; suggesting much of the normal vorticity component is vertical vorticity. This suggests that convergence into the low-level updraft amplifies pre-existing vorticity within the circuit, leading to TLV development through conservation of angular momentum. Thus, the most important role of the rotor is to cause the concentration and intense stretching (in its upward branch) of pre-existing vertical vorticity associated with the Minco mesovortex (whose vorticity was generated mostly from the tilting of horizontal vorticity along the RFGF).

Circulation analyses for longer time periods were also attempted to determine the origin of the circulation (e.g., Rotunno and Klemp 1985). However, circuits become extremely distorted with many overlapping portions and sharp discontinuities after about 90 s of backward integration (not shown), precluding any meaningful analysis.

c. The generation of the horizontal rotor and low-level updraft

While the important role the rotor plays in TLV genesis in this case has been established, the mechanism responsible for generating the rotor has not yet been examined. To help determine the mechanism, a detailed backward trajectory analysis is performed. This analysis shows that nearly all parcels within the rotor originate at very low-levels (< 125 m AGL; Fig. 11). Furthermore, our trajectory analysis suggests that almost all of the parcels that pass through the rotor came from the inflow air to the northeast of the convective cell. These parcels ascend several hundred meters over the FFGF, descend in the downward branch of the rotor while turning to the south and east, and then ascend sharply in the rotor's upward branch (Fig. 12). When plotted in three dimensional space, the typical parcel's path is helical around the rotor's central axis (Fig. 12). Inflow parcels have large values of negative y-component vorticity (the same as in the rotor) suggesting this inflow vorticity is the source of the horizontal vorticity in the rotor (see Fig. 8b). Given the proximity of these parcels to the ground, the starting location in the fairly thermodynamically-homogenous inflow area (hence, little baroclinic vorticity generation), and large values of vorticity of the opposite sign to the vorticity associated with the environmental shear, it appears likely that these parcels obtained their vorticity from surface drag. Vorticity calculations along backward trajectories that enter the rotor confirm this hypothesis as inflow parcels acquire large negative y-component vorticity from surface drag prior to entering the rotor circulation (Fig. 13).

In order to confirm that surface drag is the cause of the rotor circulation, the 100-m simulation was re-ran without the surface drag parameterization[6]. On the mesoscale, the simulation evolves in a similar manner to the experiment with surface drag, with an initial mesovortex developing and decaying, followed by the development of the Minco mesovortex (Fig. 14). However, closer examination shows that a rotor does not form, and time-height plots of maximum updraft and vertical vorticity reveal that there is no strong low-level updraft. As a result, there is no TLV in the no-drag experiment (Fig. 15). Instead, there is a long period of weaker vorticity associated with the broad rotation of the Minco mesovortex. This result strongly suggests that surface drag is the cause of the rotor and associated enhanced low-level updraft, implying that surface drag is critical to the TLV genesis in this case.

d. Analogy with rotors in the lee of mountains

Now that the importance of the rotor (and thus surface drag) in TLV genesis in this case has been established, an attempt is made to explain the mechanism by which surface drag is acting to create the rotor circulation. To do so, another atmospheric flow in which surface drag has been shown to result in the generation of rotors is examined. Namely, rotors that form on the

[6] A caveat here is, due to computational cost, the outer 400-m and 2-km domains were not re-run without surface drag. Thus, it must be assumed that impact of friction communicated to 100-m grid through the initial and boundary conditions is small. This assumption is likely valid because the features of interest are generally far from the lateral boundaries and most of the vorticity generated by friction in the 100-m experiment that included drag did not come from the initial condition, but rather was generated as the flow accelerated into the intensifying convective cell.

lee slope of mountains associated with mountain wave flows. Using idealized 2-D numerical simulations of stably stratified flow with and without surface drag, Doyle and Durran (2002) have shown that rotor formation in the lee of a mountain in a simulation with surface drag is the result of boundary layer separation that occurs as the flow turns upward into the updraft at the leading edge of the first lee-wave. Specifically, boundary layer separation occurs as the flow decelerates and is forced to rise by the adverse PGF associated with the pressure maxima beneath the lee-wave crest. As the boundary layer separates, the thin sheet of frictionally-generated vorticity near the surface is advected into the lee-wave and a rotor forms. Mountain wave simulations that do not include surface friction do not produce rotors; instead, they produce a stationary wave train that has substantially higher amplitude than the wave train in corresponding experiments that include surface friction. These results led Doyle and Durran (2002) to conclude that the rotors in their simulations formed via a synergistic interaction between boundary layer drag and trapped mountain lee-waves.

In order to compare the findings of the mountain rotor studies to our study, the following equivalencies between our study and the idealized mountain rotor scenario are noted:

(1) In both studies, there is a strong low-level wind maximum, beneath which boundary layer drag generates large values of horizontal vorticity (cf. Fig. 8b). In the mountain wave case, this vorticity maximum is caused by friction acting on the stably-stratified flow accelerating down the lee slope of the mountain. In our study, friction acting on the accelerating inflow east of the intensifying convective storm creates a similar vorticity maximum.

(2) In both studies, the atmosphere is stably stratified at low-levels. In the mountain wave case, this is specified in the initial conditions. In our case, the nocturnal nature of the

event and earlier rainfall associated with the leading convective line of the MCS lead to stable stratification of the low-level inflow (Fig. 16a). The role of stable stratification in our case is to prevent parcels from continuing to accelerate buoyantly upward after being forced to rise upon encountering the FFGF. Instead, because of stable stratification, parcels descend and become concentrated to the rear of the FFGF.

(3) Both the mountain rotor and the rotor in our simulation form just downstream of an adverse PGF that leads to boundary layer separation. As mentioned above, in the mountain wave case, this adverse PGF is just upstream of and is caused by the pressure maxima present beneath each lee-wave crest. In our case, the inflow is forced to rise by an adverse PGF associated with the pressure maximum due to the gust front. This gust front is reinforced by the westerly momentum surge (Fig. 16a) produced as the earlier mesovortex dissipates. This reinforcing surge of westerly flow increases low-level convergence which, through the diagnostic perturbation pressure equation referred to above, implies an increase in the strength of the adverse PGF and is accompanied by the rapid development and intensification of the rotor circulation (Fig. 16b). Doyle and Durran (2002) noted that rotor intensity (which they measured by the strength of the reversed flow associated with the rotor) was proportional to the strength of the adverse PGF in corresponding experiments that did not include surface drag.

While the idealized 2D mountain rotor scenario and the rotor in our simulation share many similarities, there are also important differences. Most significantly, our simulation is three-dimensional and includes flow perturbations associated with a convective storm, rather than two-dimensional and homogenous as in Doyle and Durran (2002)[7]. More specifically, pressure gradient forces associated with the convective storm and the Minco mesovortex accelerate the flow along the rotor axis and into the TLV and Minco mesovortex, leading to the formation of only one rotor instead of the series of rotors that formed in the lee of the mountain in Doyle and Durran (2002). Nonetheless, the striking similarities in the formation of the rotor, environmental conditions, and geometry of the problem (compare Fig. 17a to Fig. 17b) strongly suggests that the basic rotor formation mechanism in our simulation is largely analogous to that of the two-dimensional mountain simulations.

e. The role of surface friction in TLV genesis

It is important to make a distinction between the role of friction in TLV genesis presented herein and the role of surface drag in tornado maximum wind speed discussed in Fiedler and Rotunno (1986), Fiedler (1994), Trapp and Fiedler (1995), Grasso and Cotton (1995), and Lewellen et al. (1997). In those studies, surface drag was found to be responsible for producing a maximum wind speed in tornadoes that exceeded the so-called "thermodynamic speed limit". This occurred because surface drag led to the creation of an axial jet and supercritical end-wall vortex that made it more difficult for vortex breakdown to penetrate to the surface. Thus, these studies primarily investigated the impact of surface drag on the tornado and sub-tornado scale. This differs greatly from our study, in which surface drag has a substantial impact at the

[7] The impact of three-dimensionality was investigated in Doyle and Durran (2007), however, comparison with these results is even more difficult as three-dimensionality tends to accentuate the inherent differences between the 'flow over a mountain' and convective storm scenarios.

mesovortex scale (dramatically enhancing the mesovortex-scale updraft at low-levels). It is possible that surface drag is also acting on the tornado and sub-tornado scale in our simulation; however, this is not the focus of the present paper.

In addition to clarifying the difference between the role of surface drag on the tornado scale and the role of surface drag on the storm and mesovortex scale, we also want to expand on the role surface drag is playing in this case. In particular, it is emphasized that the primary role of the rotor in TLV genesis is the concentration and stretching of vorticity by the intense low-level updraft, not the generation of vertical vorticity from the tilting of horizontal vorticity within the rotor. Thus, a small area of intense vertical vorticity that forms within the rotor a few minutes before the TLV is examined (see the vorticity maximum near x=28.3 km, y=30.4 km in Fig. 4a). This vorticity center amplified dramatically as it moved into the intense low-level updraft (not shown). However, the small vorticity center then rapidly moves away from the ascending branch of the rotor and weakens (Fig. 4b,c). A TLV does not form until the larger area of vertical vorticity associated with the Minco mesovortex becomes coincident with the rotor. After the dissipation of the TLV, there are several brief, but intense vorticity centers that develop near, and move through the rotor (e.g., the vorticity maximum marked by a ‘Y’ in Fig. 5c). However, the strong downdraft in the eastern portion of the Minco mesovortex (see Fig. 3a) combined with the axial downdraft forced by the TLV has substantially broadened the mesovortex circulation. As such, even though the low-level updraft associated with the rotor remains intense, it is unable to re-concentrate the broad mesovortex, and no additional TLVs form in association with the small vorticity centers. Thus, the rotor and associated updraft appear to be necessary, but not sufficient, conditions for TLV genesis in the present case.

f. Summary and conceptual model

Analysis of the numerical simulations presented herein suggests a multi-step process in the development and intensification of the TLV associated with the Minco mesovortex. Fig. 18 presents a schematic of this multi-step process (for the case under consideration) and can be summarized as follows:

I) An updraft that forms at the leading of the gust front bulge tilts baroclinically generated southward pointing vortex lines upward, forming a vortex arch. Areas of cyclonic and anti-cyclonic vorticity straddle the updraft, with cyclonic (anticyclonic) rotation on the north (south) side.

II) The cyclonic vorticity intensifies along with the overall convective storm, given preference for intensification over the anti-cyclonic circulation by the presence and concentration of the background cyclonic vorticity. This intensification leads to increased low-level inflow ahead of the gust front and the generation of strong horizontal vorticity near the surface caused by surface drag.

III) The FFGF is reinforced from the rear by a surge of westerly momentum due to downdrafts from an earlier dissipating mesovortex. A horizontal rotor circulation develops and rapidly intensifies as low-level inflow and associated strong near-surface horizontal vorticity is forced to rise upon encountering the FFGF. Concurrently, the upward branch of the rotor intensifies dramatically leading to the development of an intense low-level updraft.

IV) Tornado-like vortex genesis occurs as vorticity associated with the mesovortex is concentrated and stretched by the intense low-level updraft. The vortex dissipates when a downward-directed pressure gradient force develops, inducing a downdraft at the vortex center and broadening the vortex.

5. Summary and conclusions

Although little is known about the development of quasi-linear convective system (QLCS) tornadoes, observations indicate that they tend to form in close association with strong, long-lived mesovortices. In this study, results were presented from a numerical study of one such strong, long-lived mesovortex that occurred in association with an MCS and line-end vortex on 8-9 May 2007 in central Oklahoma. The simulation was run using the ARPS model with a high-resolution (100-m grid spacing) domain nested within two larger, lower-resolution (2 km and 400 m grid spacing) domains. The two lower-resolution simulations were initialized by assimilating data from both operational WSR-88D radars and from the high-density experimental CASA radar network, as well as data from conventional sources.

The simulated mesovortex was generated in a manner consistent with the development mechanism for mesovortex couplets proposed by Atkins and St. Laurent (2009b). Namely, cyclonic and anticyclonic vortex couplets formed on either side of an enhanced updraft associated with a bulging gust front. The cyclonic member of the vortex couplets strengthened and persisted for ~ 1 hr. The simulated mesovortex produced a strong low-level sub-mesovortex scale tornado-like vortex (TLV). Closer inspection of the genesis of this TLV showed that a strong low-level updraft was critical for the convergence and amplification of the vertical vorticity associated with this mesovortex to tornado strength. This low-level updraft was found to be the upward branch of a strong horizontal rotor located just to the northwest of the TLV. The cause of the rotor was shown to be the interaction between the convective outflow and frictionally-generated near-ground horizontal vorticity underneath enhanced low-level storm inflow.

The results presented herein come with a common caveat to studies focusing on high-resolution numerical simulation; that is, they are only explicitly valid for this one case and may be limited by the experiment design (resolution, etc.). However, an important aspect of this study is that, as far as we know, it is the first to highlight the existence and importance of the rotor circulation and show a possible substantial impact of surface drag on the storm and sub-storm scale [rather than on the sub-tornado scale (e.g., Fiedler 1994)]. It is also one of few studies of this type whose simulated storms are initialized using real data and in which the model simulations verify reasonably with observations. Our findings are also consistent with earlier studies that showed tornadoes within QLCSs are typically associated with strong, long-lived mesovortices. In our study, a critical ingredient for rotor development is the frictional generation of near-surface horizontal vorticity associated with the intensification of the inflow into the Minco mesovortex. This flow profile takes about 10 min to develop after the genesis of the Minco mesovortex. We speculate that weaker, shorter lived mesovortices may dissipate before a rotor-circulation develops, which could preclude tornadogenesis.

The important role of surface drag and the rotor circulation raises a number of questions that will be the focus of future work. Most importantly, how common is a rotor feature in tornadic mesovortices associated with QLCSs? It seems probable that the environment of our simulation is at least somewhat typical of environments associated with many QLCSs. Is a similar rotor type feature common and/or important in supercell tornadogenesis? Dowell and Bluestein (1997) found very strong shear in wind observations from a 440-m tall instrumented tower in near-updraft supercell inflow (see their Fig. 18). They speculated that this shear may have been caused by stretching of baroclinic vorticity associated with anvil shading. However, numerical simulations investigating the impact of anvil shading (Frame and Markowski 2010) showed that a similar shear profile was the result of surface drag slowing the near-ground flow. Additionally, an examination of dual-Doppler and mobile mesonet data from the Goshen County, Wyoming, 5 June 2009 supercell intercepted during the VORTEX2 project suggests that surface drag cannot be ruled out as a contributor to positive circulation (Markowski 2012a, b). It seems probable that the only way to answer these questions will be through additional high-resolution simulations of different cases as, even in targeted field campaigns, near ground (~200 m AGL or below) high-resolution observations are generally not available. Such simulations will be the subject for future research.

Acknowledgements: This work was primarily supported by NSF grants EEC-0313747 and AGS-0802888. The second author was also supported by NSF grants OCI-0905040, AGS-0750790., AGS-0941491, AGS-1046171, and AGS-1046081. Numerical simulations were performed at the University of Oklahoma Supercomputing Center for Education and Research (OSCER). Matt Kumjian is thanked for a thorough review of this manuscript. The first author also wishes to thank Brett Roberts, Daniel Betten, Dan Dawson, and Jeff Trapp for help and insightful conversations about a variety of topics related to this study. Thorough and thoughtful reviews from three anonymous reviewers helped to strengthen the content of this manuscript.

References

Atkins, N. T., J. M. Arnott, R. W. Przybylinski, R. A. Wolf, and B. D. Ketcham, 2004: Vortex structure and evolution within bow echoes. Part I: Single-Doppler and damage analysis of the 29 June 1998 derecho. . *Mon. Wea. Rev.*, **132,** 2224-2242.

Atkins, N. T., C. S. Bouchard, R. W. Przybylinski, R. J. Trapp, and G. Schmocker, 2005: Damaging surface wind mechanisms within the 10 June 2003 Saint Louis bow echo during BAMEX. . *Mon. Wea. Rev.*, **133,** 2275-2296.

Atkins, N. T. and M. St. Laurent, 2009a: Bow echo mesovortices. Part I: Processes that influence their damaging potential. . *Mon. Wea. Rev.*, **137,** 1497-1513.

Atkins, N. T. and M. S. Laurent, 2009b: Bow echo mesovortices. Part II: Their genesis. *Mon. Wea. Rev.*, **137,** 1514-1532.

Chen, F. and J. Dudhia, 2001: Coupling an advanced land surface-hydrology model with the Penn State-NCAR MM5 modeling system. Part I: Model implementation and sensitivity. *Mon. Wea. Rev.*, **129,** 569.

Davis, C., N. Atkins, D. Bartels, L. Bosart, M. Coniglio, G. Bryan, W. Cotton, D. Dowell, B. Jewett, R. Johns, D. Jorgensen, J. Knievel, K. Knupp, W.-C. Lee, G. McFarquhar, J. Moore, R. Przybylinski, R. Rauber, B. Smull, R. Trapp, S. Trier, R. Wakimoto, M. Weisman, and C. Ziegler, 2004: The bow echo and MCV experiment: Observations and opportunities. *Bulletin of the American Meteorological Society*, **85,** 1075-1093.

Dowell, D. C. and H. B. Bluestein, 1997: The Arcadia, Oklahoma, storm of 17 May 1981: Analysis of a supercell during tornadogenesis. *Mon. Wea. Rev.*, **125,** 2562-2582.

Doyle, J. and D. R. Durran, 2002: The dynamics of mountain-wave induced rotors. *J. Atmos. Sci.*, **59,** 186-201.

Doyle, J. and D. R. Durran, 2007: Rotor and subrotor dynamics in the lee of three-dimensional terrain. *J. Atmos. Sci.*, **64,** 4202–4221.

Fiedler, B., 1994: The thermodynamic speed limit and its violation in axisymmetric numerical simulations of tornado-like vortices. *Atmos. Ocean*, **32,** 335-359.

Fiedler, B. H. and R. Rotunno, 1986: A theory for the maximum windspeeds in tornado-like vortices. *J. Atmos. Sci.*, **43,** 2328-2340.

Forbes, G. S. and R. M. Wakimoto, 1983: A concentrated outbreak of tornadoes, downbursts and microbursts, and implications regarding vortex classification. *Mon. Wea. Rev.*, **111,** 220-235.

Frame, J. and P. M. Markowski, 2010: Numerical simulations of radiative cooling beneath the anvils of supercell thunderstorms. *Mon. Wea. Rev.*, **138,** 3024-3047.

Fujita, T., 1978: Manual of downburst identification for project NIMROD, 104 pp pp.

Grasso, L. D. and W. R. Cotton, 1995: Numerical simulation of a tornado vortex. *J. Atmos. Sci.*, **52,** 1192-1203.

Lemon, L. R. and C. A. Doswell, 1979: Severe thunderstorm evolution and mesocyclone structure as related to tornadogenesis. *Mon. Wea. Rev.*, **107,** 1184-1197.

Lewellen, W. S., D. C. Lewellen, and R. I. Sykes, 1997: Large-eddy simulation of a tornado's interaction with the surface. *J. Atmos. Sci.*, **54,** 581-605.

Lin, Y.-L., R. D. Farley, and H. D. Orville, 1983: Bulk parameterization of the snow field in a cloud model. *J. Climat. Appl. Meteor.*, **22,** 1065-1092.

Markowski, P., Y. Richardson, J. Marquis, J. Wurman, K. Kosiba, P. Robinson, D. Dowell, E. Rasmussen, and R. Davies-Jones, 2012a: The pretornadic phase of the Goshen County, Wyoming, supercell of 5 June 2009 intercepted by VORTEX2. Part I: Evolution of kinematic and surface thermodynamic fields. *Mon. Wea. Rev.***,** in press.

Markowski, P., Y. Richardson, J. Marquis, J. Wurman, K. Kosiba, P. Robinson, D. Dowell, E. Rasmussen, and R. Davies-Jones, 2012b: The pretornadic phase of the Goshen County, Wyoming, supercell of 5 June 2009 intercepted by VORTEX2. Part II: Intensification of low-level rotation. . *Mon. Wea. Rev.***,** in press.

Markowski, P. M., M. Majcen, Y. Richardson, J. Marquis, and J. Wurman, 2011: Characteristics of the wind field in a trio of nontornadic low-level mesocyclones observed by the doppler on wheels radars. *Electronic J. Severe Storms Meteor.*, **6 (3),** 1-48.

Markowski, P. M., E. Rasmussen, J. Straka, R. Davies-Jones, Y. Richardson, and R. J. Trapp, 2008: Vortex lines within low-level mesocyclones obtained from pseudo-dual-Doppler radar observations. *Mon. Wea. Rev.*, **136,** 3513-3535.

Markowski, P. M. and Y. Richardson, 2010: *Mesoscale meteorology in midlatitudes.* Wiley, 430 pp.

McLaughlin, D., D. Pepyne, V. Chandrasekar, B. Philips, J. Kurose, M. Zink, K. Droegemeier, S. Cruz-Pol, F. Junyent, J. Brotzge, D. Westbrook, N. Bharadwaj, Y. Wang, E. Lyons, K. Hondl, Y. Liu, E. Knapp, M. Xue, A. Hopf, K. Kloesel, A. DeFonzo, P. Kollias, K. Brewster, R. Contreras, B. Dolan, T. Djaferis, E. Insanic, S. Frasier, and F. Carr, 2009: Short-wavelength technology and the potential for distributed networks of small radar systems. *Bulletin of the American Meteorological Society*, **90,** 1797-1817.

Orlanski, I., 1975: A rational subdivision of scales for atmospheric processes. *Bulletin of the American Meteorological Society*, **56,** 527-530.

Przybylinski, R. W., 1995: The bow echo: Observations, numerical simulations, and severe weather detection methods. *Wea. and Forecasting,* **10,** 203-218.

Rotunno, R. and J. B. Klemp, 1985: On the rotation and propagation of simulated supercell thunderstorms. *J. Atmos. Sci.*, **42,** 271-292.

Schenkman, A., M. Xue, A. Shapiro, K. Brewster, and J. Gao, 2011a: Impact of CASA radar and Oklahoma mesonet data assimilation on the analysis and prediction of tornadic mesovortices in a MCS. *Mon. Wea. Rev.*, **139,** 3422-3445.

Schenkman, A., M. Xue, A. Shapiro, K. Brewster, and J. Gao, 2011b: The analysis and prediction of the 8-9 May 2007 Oklahoma tornadic mesoscale convective system by assimilating WSR-88D and CASA radar data using 3DVAR. *Mon. Wea. Rev.*, **139,** 224-246.

Snook, N. and M. Xue, 2008: Effects of microphysical drop size distribution on tornadogenesis in supercell thunderstorms. *Geophy. Res. Letters*, **35,** L24803, doi:10.1029/2008GL035866.

Straka, J. M., E. N. Rasmussen, R. P. Davies-Jones, and P. M. Markowski, 2007: An observational and idealized numerical examination of low-level counter-rotating vortices in the rear flank of supercells. *Electronic J. Severe Storms Meteor.*, **2 (8),** 1-22.

Trapp, R. J. and B. Fiedler, 1995: Tornado-like vortexgenesis in a simplified numerical model. *J. Atmos. Sci.*, **52,** 3757-3778.

Trapp, R. J., S. A. Tessendorf, E. S. Godfrey, and H. E. Brooks, 2005: Tornadoes from squall lines and bow echoes. Part I: Climatological distribution. *Wea. Forecasting*, **20,** 23-34.

Trapp, R. J. and M. L. Weisman, 2003: Low-level mesovortices within squall lines and bow echoes. Part II: Their genesis and implications. *Mon. Wea. Rev.*, **131,** 2804-2823.

Wakimoto, R. M., H. V. Murphey, C. A. Davis, and N. T. Atkins, 2006a: High winds generated by bow echoes. Part II: The relationship between the mesovortices and damaging straight-line winds. *Mon. Wea. Rev.*, **134,** 2813-2829.

Wakimoto, R. M., H. V. Murphey, A. Nester, D. P. Jorgensen, and N. T. Atkins, 2006b: High winds generated by bow echoes. Part I: Overview of the Omaha bow echo 5 July 2003 storm during BAMEX. *Mon. Wea. Rev.*, **134,** 2793-2812.

Weisman, M. L. and C. A. Davis, 1998: Mechanisms for the generation of mesoscale vortices within quasi-linear convective systems. *J. Atmos. Sci.*, **55,** 2603-2622.

Weisman, M. L. and R. J. Trapp, 2003: Low-level mesovortices within squall lines and bow echoes. Part I: Overview and dependence on environmental shear. *Mon. Wea. Rev.*, **131,** 2779-2803.

Wheatley, D. M. and R. J. Trapp, 2008: The effect of mesoscale heterogeneity on the genesis and structure of mesovortices within quasi-linear convective systems. *Mon. Wea. Rev.*, **136,** 4220-4241.

Wheatley, D. M., R. J. Trapp, and N. T. Atkins, 2006: Radar and damage analysis of severe bow echoes observed during BAMEX. *Mon. Wea. Rev.*, **134,** 791-806.

Xue, M., K. K. Droegemeier, and V. Wong, 2000: The Advanced Regional Prediction System (ARPS) - A multiscale nonhydrostatic atmospheric simulation and prediction tool. Part I: Model dynamics and verification. *Meteor. Atmos. Physics,* **75,** 161-193.

Xue, M., K. K. Droegemeier, V. Wong, A. Shapiro, and K. Brewster, 1995: *ARPS Version 4.0 User's Guide*. [Available at http://www.caps.ou.edu/ARPS], 380 pp.

Xue, M., K. K. Droegemeier, V. Wong, A. Shapiro, K. Brewster, F. Carr, D. Weber, Y. Liu, and D. Wang, 2001: The Advanced Regional Prediction System (ARPS) - A multi-scale nonhydrostatic atmospheric simulation and prediction tool. Part II: Model physics and applications. *Meteor. Atmos. Phys.*, **76,** 143-166.

Xue, M., D.-H. Wang, J.-D. Gao, K. Brewster, and K. K. Droegemeier, 2003: The Advanced Regional Prediction System (ARPS), storm-scale numerical weather prediction and data assimilation. *Meteor. Atmos. Physics*, **82,** 139-170.

List of figures

Fig. 1. Map of observed radar reflectivity factor at 1 km AGL at 0350 UTC 9 May 2007 within the 2-km resolution computational domain used in Schenkman et al. (2011a). The dashed-line rectangle marks the location of the 400-m resolution domain used in S11a. The image at the upper-right zooms into the 400-m domain. The solid rectangle marks the location of 100-m resolution computational domain. The oval contains the convective cell associated with the Minco mesovortex. The location of the LEV and selected town names are indicated.

Fig. 2 Equivalent potential temperature (shaded, K), horizontal wind (vectors, m s^{-1}), positive vertical vorticity >0.025 s^{-1} (shaded in red), negative vertical vorticity < -0.025 s^{-1} (shaded in blue) at 100-m AGL and vertical velocity (> 5 m s^{-1}, heavy green contours) at 750-m AGL at (a) 0300 UTC, (b) 0305 UTC, and (c) 0315 UTC 9 May 2007. The heavy black line in (a) marks the gust front. For clarity, this line is neglected in (b) and (c). In (b) “couplets” is put in quotation marks to imply that while there are not well defined vorticity couplets, there is predominantly positive (negative) vorticity on the northern (southern) side of the gust front bulge. A vortex line, calculated from the 3D vorticity vector field and color coded by height AGL, is plotted in (b).

Fig. 3. Vertical velocity (m s^{-1}, shaded) and horizontal wind (m s^{-1}, vectors) at 1000 m AGL at (a) 0330 UTC and (b) 0340 UTC 9 May 2007. ‘M’ marks the approximate center of the Minco mesovortex.

Fig. 4. Horizontal wind vectors (m s^{-1}) and vertical vorticity (color shaded, s^{-1}) at 20 m AGL at (a) 0325:30 UTC, (b) 0326:00 UTC, (c) 0326:30 UTC, (d) 0327:00 UTC, (e) 0327:30 UTC, and (f) 0328:00 UTC 9 May 2007. The ‘X’ in (a-c) marks the location of a small

area of cyclonic vorticity that merges with the TLV. The ‘T’ in (e-f) marks the location of the TLV. The solid and dotted black lines mark the locations of the rear and forward flank gust fronts, respectively. These gust fronts are hand-analyzed through the relative maximum in convergence.

Fig. 5. As Fig. 4 but at (a) 0329 UTC, (b) 0331 UTC, (c) 0333 UTC, and (d) 0335 UTC. Dashed contours are perturbation pressure (hPa, starting at -3 hPa). The minimum perturbation pressure is ~-12.6 hPa in the center of the TLV in (a). The ‘Y’ in (c) marks a short-lived area of vorticity that forms after the demise of the TLV. Gust fronts are neglected because they have moved out of the plotted area by 0331 UTC.

Fig. 6. Time-height profiles of (a) maximum vertical velocity (m s^{-1}) and (b) vertical vorticity (s^{-1}) from 0300 to 0342 UTC. Profiles are calculated over a 32 x 42 km subdomain that is centered on the Minco mesovortex and excludes an additional storm in the southeast portion of the domain. The subdomain is chosen to be fairly large in order to include both the mid-level and low-level updrafts through the entire 42 min period. The dotted oval marks the intense low-level updraft located on the west side of the Minco mesovortex.

Fig. 7. Vertical vorticity budget along a representative backward trajectory that is initialized 100 m AGL near the TLV center at 0328 UTC. The blue line is the sum of the time-integrated vertical vorticity generated through vertical stretching (red line) and tilting (green line). The cyan line represents the vertical vorticity interpolated from the model grid to the location of the parcel at each time. Trajectories are calculated using a 4^{th} order Runge-Kutta integration scheme with 3 s model output. The Lagrangian time integration agrees very well with the Eulerian vorticity prediction by the model in this case.

Fig. 8. (a) Vertical velocity (shaded, m s^{-1}) at 0329 UTC at 500 m AGL overlaid with horizontal wind (vectors, m s^{-1}) and convergence (s^{-1}) at 20 m AGL. The large black arrows indicate the direction of flow behind the FFGF (dotted blue line) and RFGF (solid blue line) (b) Cross-section along the heavy black line in (a) and (c). Y-component vorticity (shaded, s^{-1}), perturbation pressure (dashed contours, hPa) and wind vectors are plotted in the plane of the cross-section. The large black arrow indicates the location of the strong low-level updraft. (c) Y-component vorticity (shaded, s^{-1}) , perturbation pressure (dashed contours, hPa) and horizontal wind (vectors, m s^{-1}) at 500 m AGL. A 600-m diameter ring of backward trajectories (gray lines) that enter the TLV circulation at 500 m AGL are overlaid in (c). The ‘T’ in (a) and (c) marks the approximate TLV center.

Fig. 9. Tilting of horizontal vorticity into the vertical (shaded, s^{-2}), vertical vorticity (contours, s^{-1}), and horizontal wind vectors (m s^{-1}) at 300 m AGL at 03:25:30 UTC. The ‘X’ marks the location of the small vertical vorticity maximum highlighted in Fig. 4.

Fig. 10. Circulation (black line) around the material circuit (shown in the inset) that was initially (at 0328 UTC) a 200-m radius circle surrounding the TLV 100-m AGL. The circuit is made up of 3600 parcels.

Fig. 11. Height AGL that a parcel in a present location at 0329 UTC was located at 0319 UTC (shaded, m AGL), together with the negative Y-component vorticity with a contour interval of 0.02 s^{-1} beginning at -0.04 s^{-1} (red contours), and the wind vectors in an east-west cross-section plane (m s^{-1}) along the black line in Fig. 8a.

Fig. 12. Three dimensional plot (view from the south-southeast) of a typical parcel trajectory traveling through the rotor beginning at 0312:30 UTC and terminating in the rotor’s upward branch at 0327:30 UTC. The inset is a XY cross-section plot of the y-component

of horizontal vorticity (shaded, s^{-1}) at 0327:30 UTC overlaid with the two-dimensional projection of the trajectory. Dots along the trajectory are color coded by height AGL (m).

Fig. 13. Y-component vorticity budget for the parcel plotted in Fig. 12, but integrated backward in time until 0305:30 UTC. The parcel enters the rotor around 0320:00 UTC. The gray solid line is the sum of the time-integrated stretching (short dashed gray line), tilting (short dashed black line), frictional generation (alternating short-long black dashed line) and baroclinic generation (long dashed gray line). The solid black line represents y-component vorticity interpolated to the parcel location from the model grid at each time.

Fig. 14. As Fig. 2 but for the experiment with surface drag turned off and only at (a) 0305 UTC and (b) 0315 UTC.

Fig. 15. As Fig. 6 but for the experiment with the surface drag parameterization turned off.

Fig. 16. Perturbation pressure (shaded, hPa), perturbation potential temperature (blue contours, K), and velocity in the plane of the cross-section (vectors, m s^{-1}) at (a) 0320 UTC and (b) 0325 UTC 9 May 2007. The 'W' in (a) marks the leading edge of the westerly momentum surge associated with the decaying initial mesovortex. The red-outlined arrows in (b) give the sense of the PGF direction.

Fig. 17. Y-component vorticity (shaded, s^{-1}) and velocity vectors in the plane of the cross-section (vectors, m s^{-1}) from (a) an XZ crossection through the rotor at 0325 UTC and (b) from a XZ cross-section through a simulated rotor in the lee of a mountain [adapted from Doyle and Durran (2007)]. In (b), the original figure of Doyle and Durran (2007) has been reflected about the x-axis in order to directly compare with the flow geometry of the rotor in the 9 May 2007 case.

Fig. 18. Schematic of four-stage process leading up to TLV genesis. Vertical vorticity couplet development is depicted in (I). (II) shows the development of the dominant cyclonic Minco mesovortex and the associated development of frictionally-generated horizontal vorticity. (III) illustrates the development of the rotor. TLV genesis is shown in (IV). The cyan shading represents the cold pool. The dark blue shading represents the cold air within the cold pool bulge. Black arrows represent the surface flow trajectories. The orange arrows represent trajectories which enter the main updraft. The purple arrow in (III) and (IV) marks the horizontal rotor axis. The magenta arrows represent parcel trajectories that enter the rotor. Light gray vectors are idealized vortex lines. The 'M' represents the location of the Minco mesovortex. The dotted curves in (II) and (III) mark the location of the enhanced westerly momentum associated with the dissipation of the initial mesovortex. The 'v' behind the outflow surge from the initial mesovortex in (III) marks the location of the small area of vertical vorticity moving through the rotor. The 'T' in (IV) marks the location of the TLV.

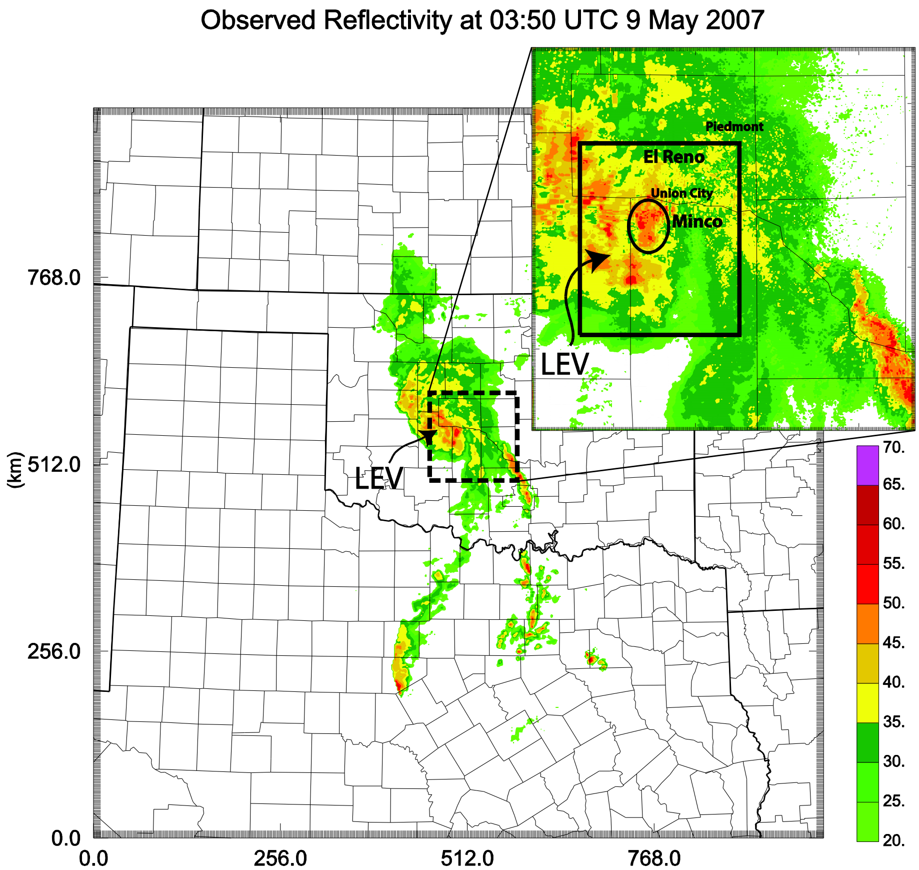

Fig. 1. Map of observed radar reflectivity factor at 1 km AGL at 0350 UTC 9 May 2007 within the 2-km resolution computational domain used in Schenkman et al. (2011a). The dashed-line rectangle marks the location of the 400-m resolution domain used in S11a. The image at the upper-right zooms into the 400-m domain. The solid rectangle marks the location of 100-m resolution computational domain. The oval contains the convective cell associated with the Minco mesovortex. The location of the LEV and selected town names are indicated.

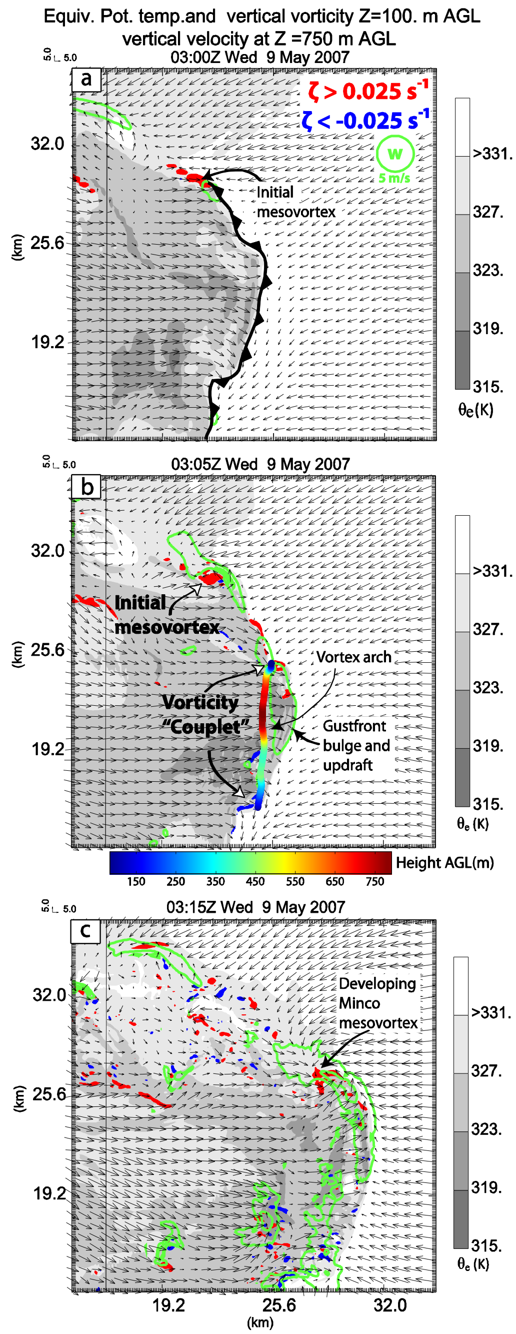

Fig. 2 Equivalent potential temperature (shaded, K), horizontal wind (vectors, m s $^{-1}$), positive vertical vorticity >0.025 s^{-1} (shaded in red), negative vertical vorticity < -0.025 s^{-1} (shaded in blue) at 100-m AGL and vertical velocity (> 5 m s^{-1}, heavy green contours) at 750-m AGL at (a) 0300 UTC, (b) 0305 UTC, and (c) 0315 UTC 9 May 2007. The heavy black line in (a) marks the gust front. For clarity, this line is neglected in (b) and (c). In (b) "couplets" is put in quotation marks to imply that while there are not well defined vorticity couplets, there is predominantly positive (negative) vorticity on the northern (southern) side of the gust front bulge. A vortex line, calculated from the 3D vorticity vector field and color coded by height AGL, is plotted in (b).

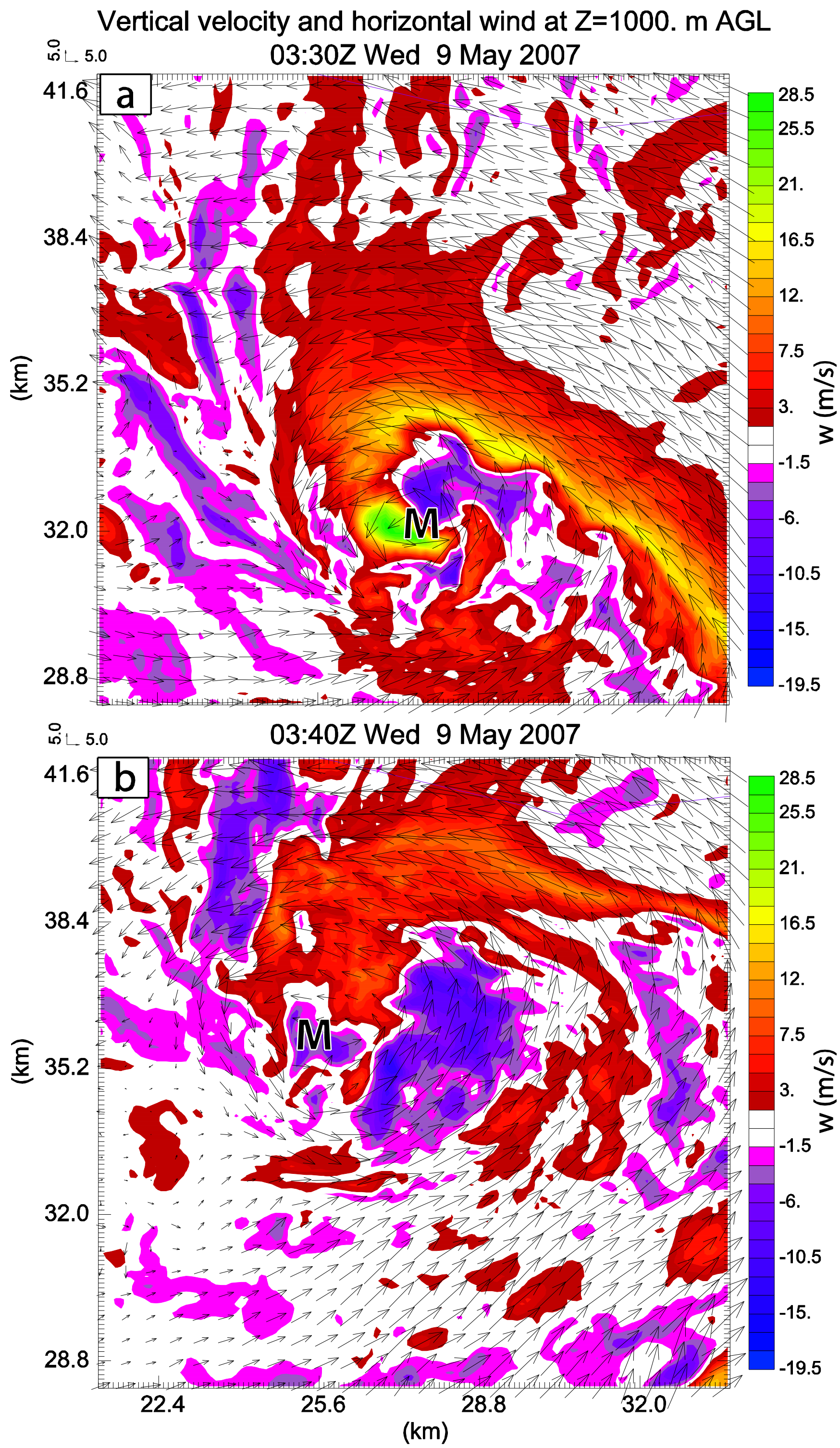

Fig. 3. Vertical velocity (m s^{-1}, shaded) and horizontal wind (m s^{-1}, vectors) at 1000 m AGL at (a) 0330 UTC and (b) 0340 UTC 9 May 2007. ‘M’ marks the approximate center of the Minco mesovortex.

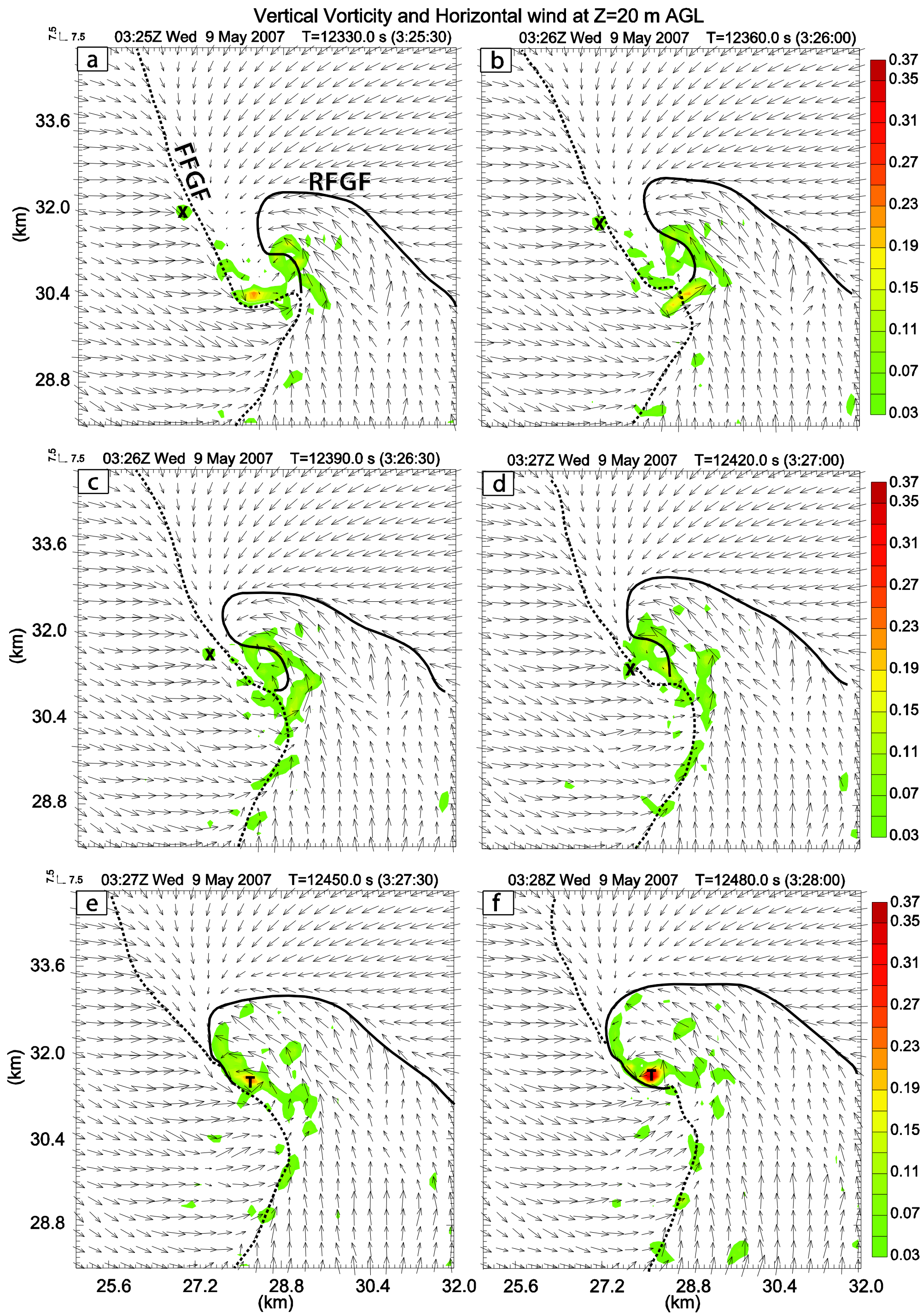

Fig. 4. Horizontal wind vectors (m s $^{-1}$) and vertical vorticity (color shaded, s^{-1}) at 20 m AGL at (a) 0325:30 UTC, (b) 0326:00 UTC, (c) 0326:30 UTC, (d) 0327:00 UTC, (e) 0327:30 UTC, and (f) 0328:00 UTC 9 May 2007. The 'X' in (a-c) marks the location of a small area of cyclonic vorticity that merges with the TLV. The 'T' in (e-f) marks the location of the TLV. The solid and dotted black lines mark the locations of the rear and forward flank gust fronts, respectively. These gust fronts are hand-analyzed through the relative maximum in convergence.

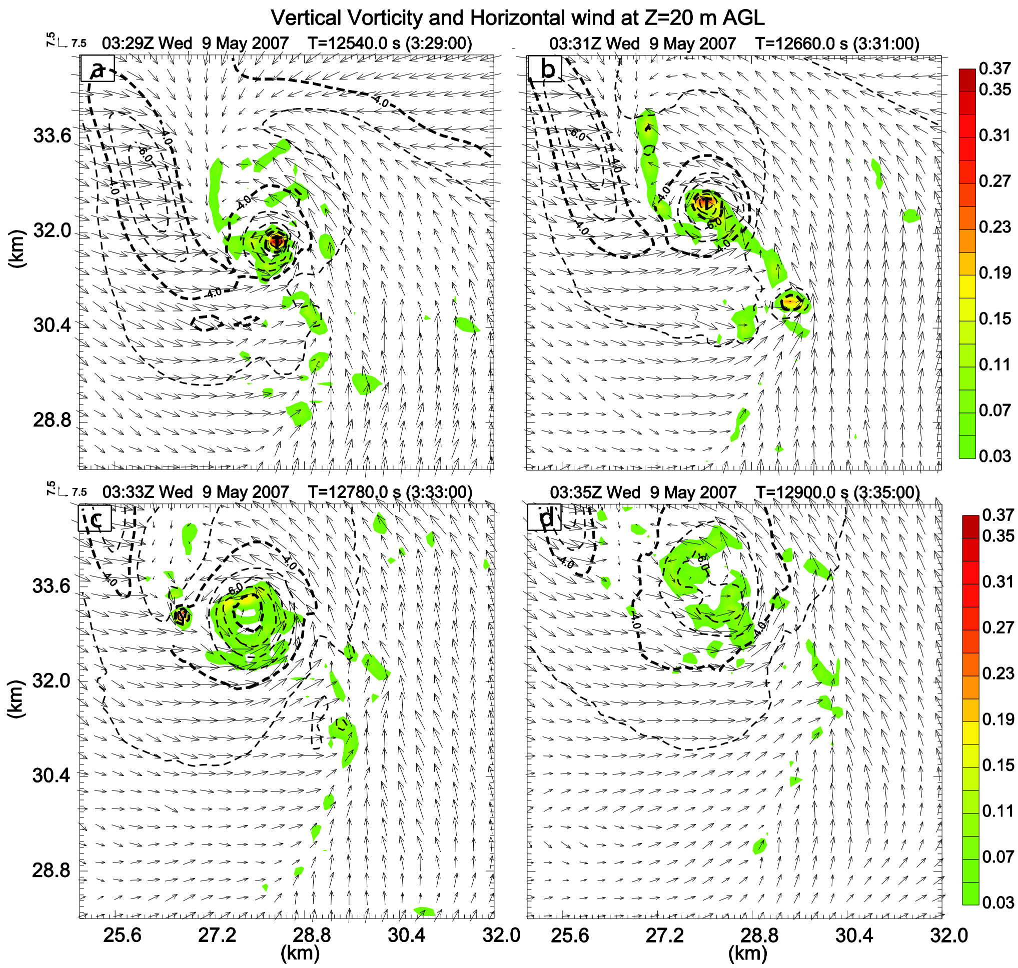

Fig. 5. As Fig. 4 but at (a) 0329 UTC, (b) 0331 UTC, (c) 0333 UTC, and (d) 0335 UTC. Dashed contours are perturbation pressure (hPa, starting at -3 hPa). The minimum perturbation pressure is ~-12.6 hPa in the center of the TLV in (a). The 'Y' in (c) marks a short-lived area of vorticity that forms after the demise of the TLV. Gust fronts are neglected because they have moved out of the plotted area by 0331 UTC.

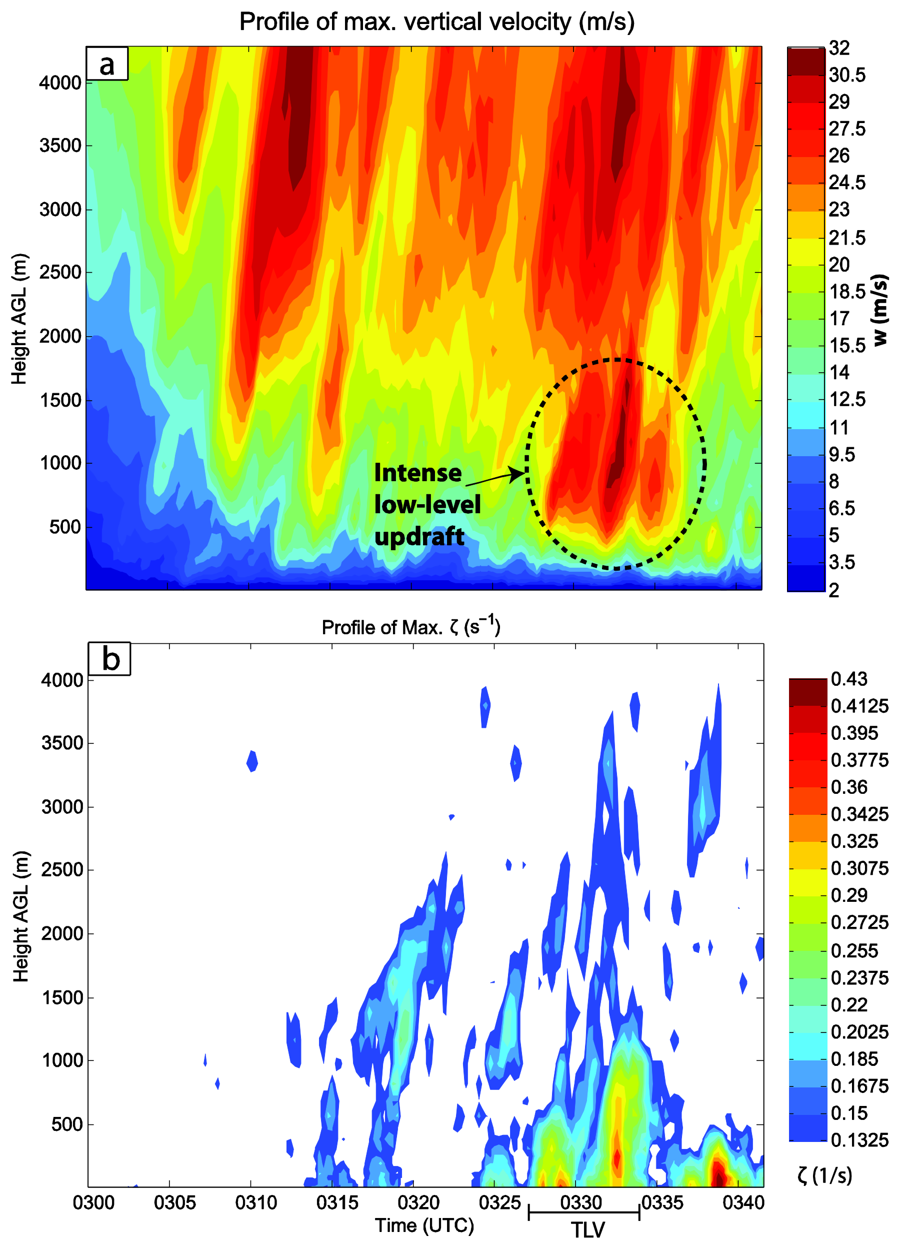

\

Fig. 6. Time-height profiles of (a) maximum vertical velocity (m s^{-1}) and (b) vertical vorticity (s^{-1}) from 0300 to 0342 UTC. Profiles are calculated over a 32 x 42 km subdomain that is centered on the Minco mesovortex and excludes an additional storm in the southeast portion of the domain. The subdomain is chosen to be fairly large in order to include both the mid-level and low-level updrafts through the entire 42 min period. The dotted oval marks the intense low-level updraft located on the west side of the Minco mesovortex.

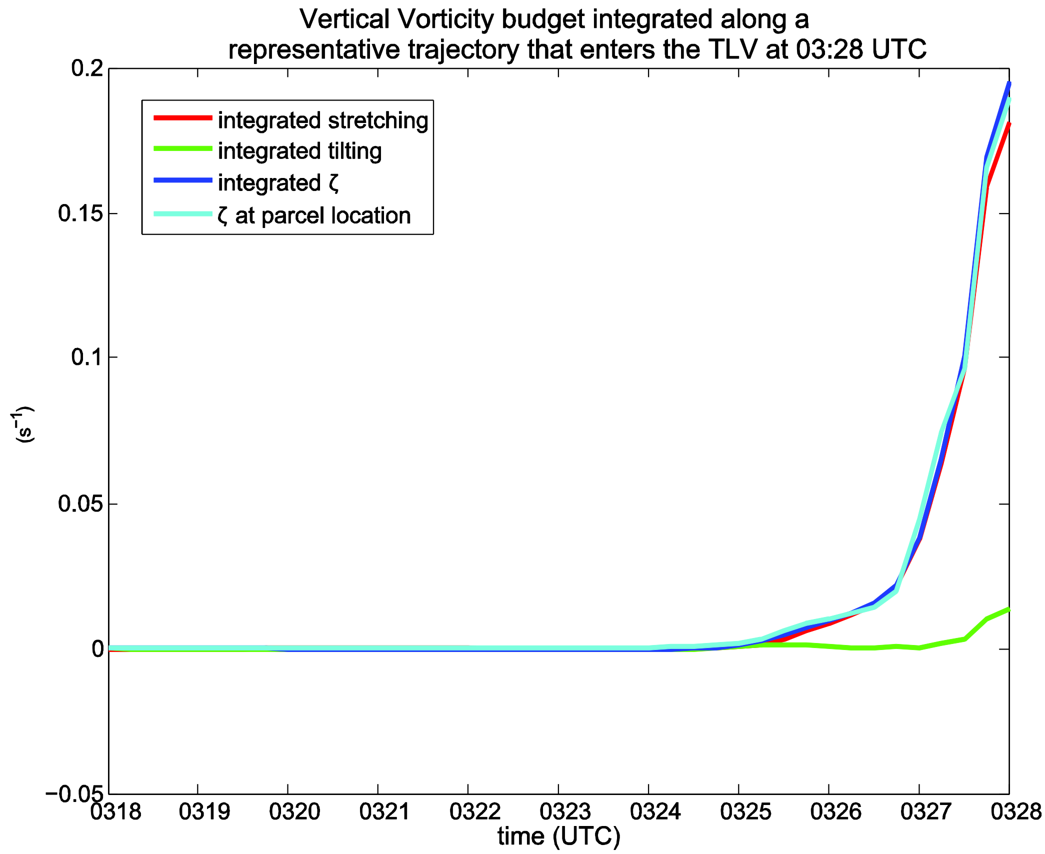

Fig. 7. Vertical vorticity budget along a representative backward trajectory that is initialized 100 m AGL near the TLV center at 0328 UTC. The blue line is the sum of the time-integrated vertical vorticity generated through vertical stretching (red line) and tilting (green line). The cyan line represents the vertical vorticity interpolated from the model grid to the location of the parcel at each time. Trajectories are calculated using a 4th order Runge-Kutta integration scheme with 3 s model output. The Lagrangian time integration agrees very well with the Eulerian vorticity prediction by the model in this case.

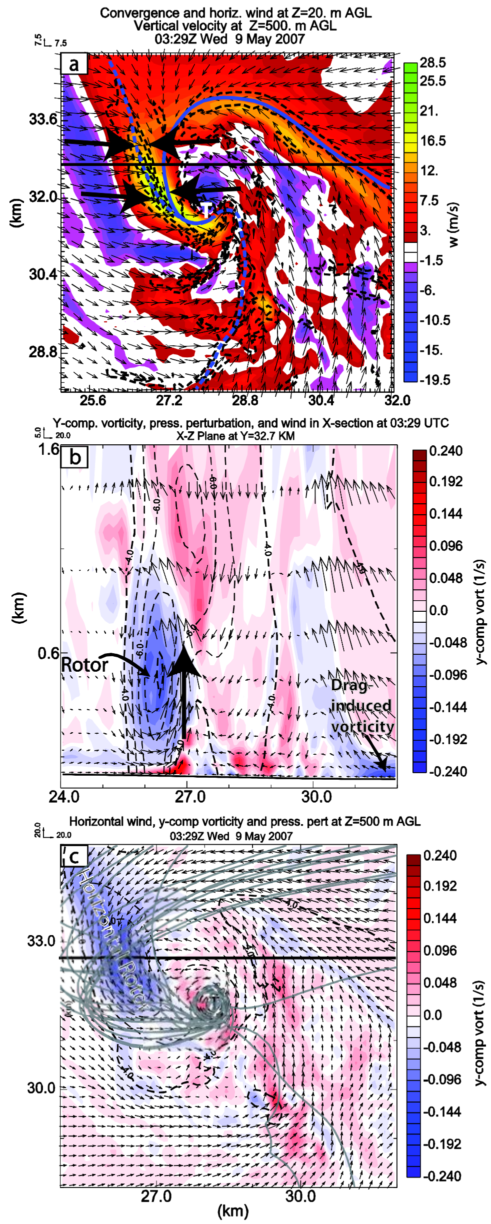

Fig. 8. (a) Vertical velocity (shaded, m s^{-1}) at 0329 UTC at 500 m AGL overlaid with horizontal wind (vectors, m s^{-1}) and convergence (s^{-1}) at 20 m AGL. The large black arrows indicate the direction of flow behind the FFGF (dotted blue line) and RFGF (solid blue line) (b) Cross-section along the heavy black line in (a) and (c). Y-component vorticity (shaded, s^{-1}), perturbation pressure (dashed contours, hPa) and wind vectors are plotted in the plane of the cross-section. The large black arrow indicates the location of the strong low-level updraft. (c) Y-component vorticity (shaded, s^{-1}) , perturbation pressure (dashed contours, hPa) and horizontal wind (vectors, m s^{-1}) at 500 m AGL. A 600-m diameter ring of backward trajectories (gray lines) that enter the TLV circulation at 500 m AGL are overlaid in (c). The 'T' in (a) and (c) marks the approximate TLV center.

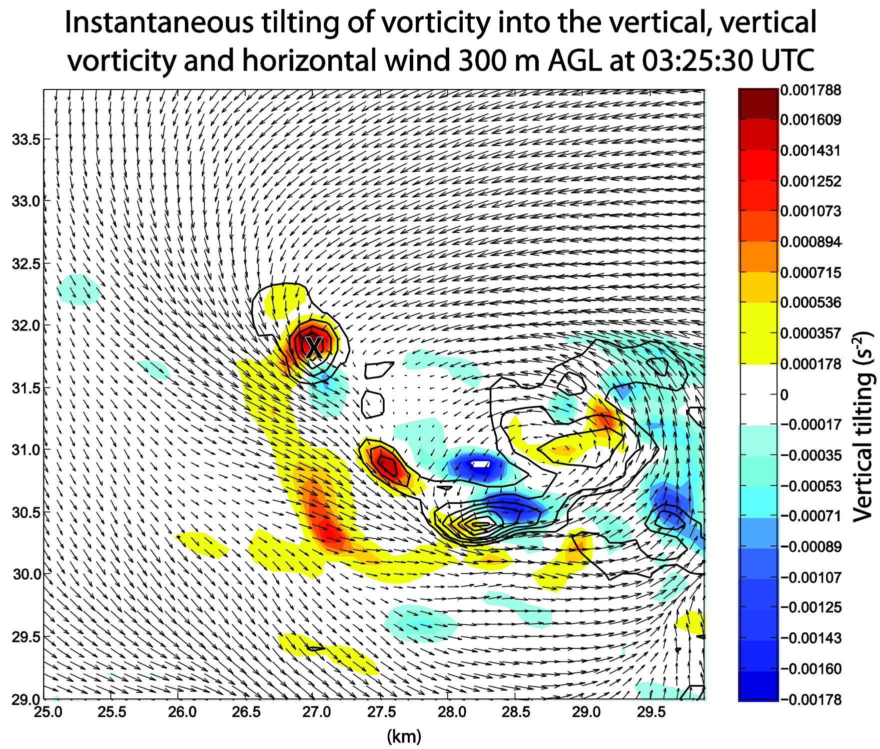

Fig. 9. Tilting of horizontal vorticity into the vertical (shaded, s^{-2}), vertical vorticity (contours, s^{-1}), and horizontal wind vectors ($m\ s^{-1}$) at 300 m AGL at 03:25:30 UTC. The ‘X’ marks the location of the small vertical vorticity maximum highlighted in Fig. 4.

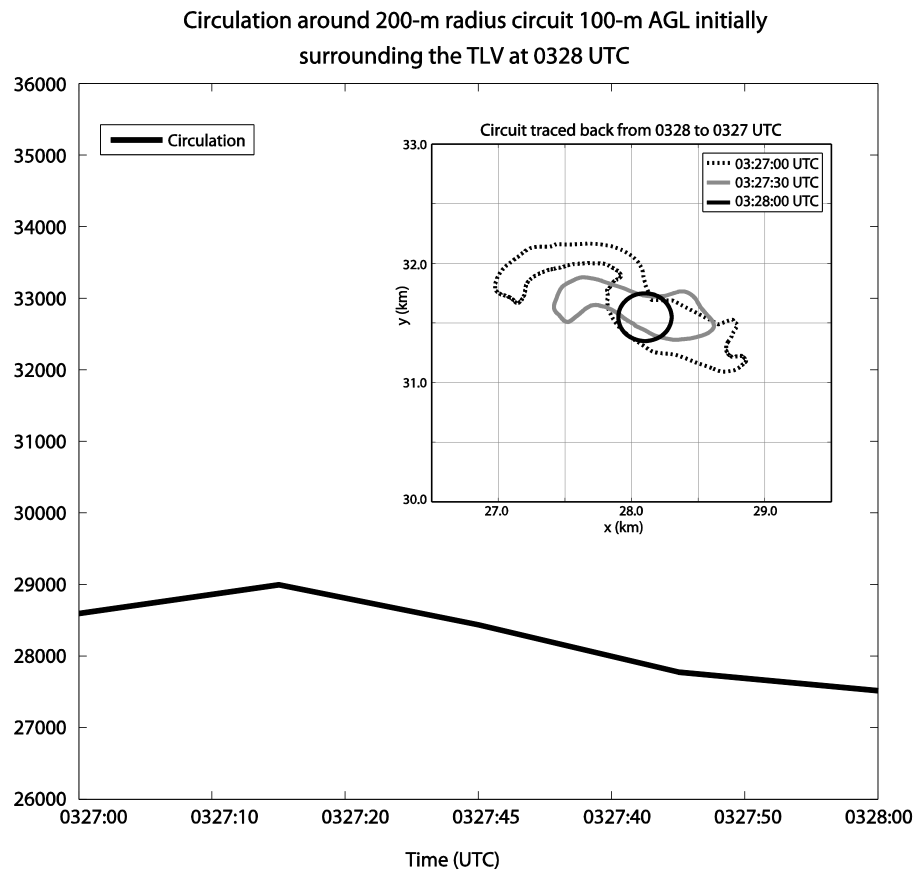

Fig. 10. Circulation (black line) around the material circuit (shown in the inset) that was initially (at 0328 UTC) a 200-m radius circle surrounding the TLV 100-m AGL. The circuit is made up of 3600 parcels.

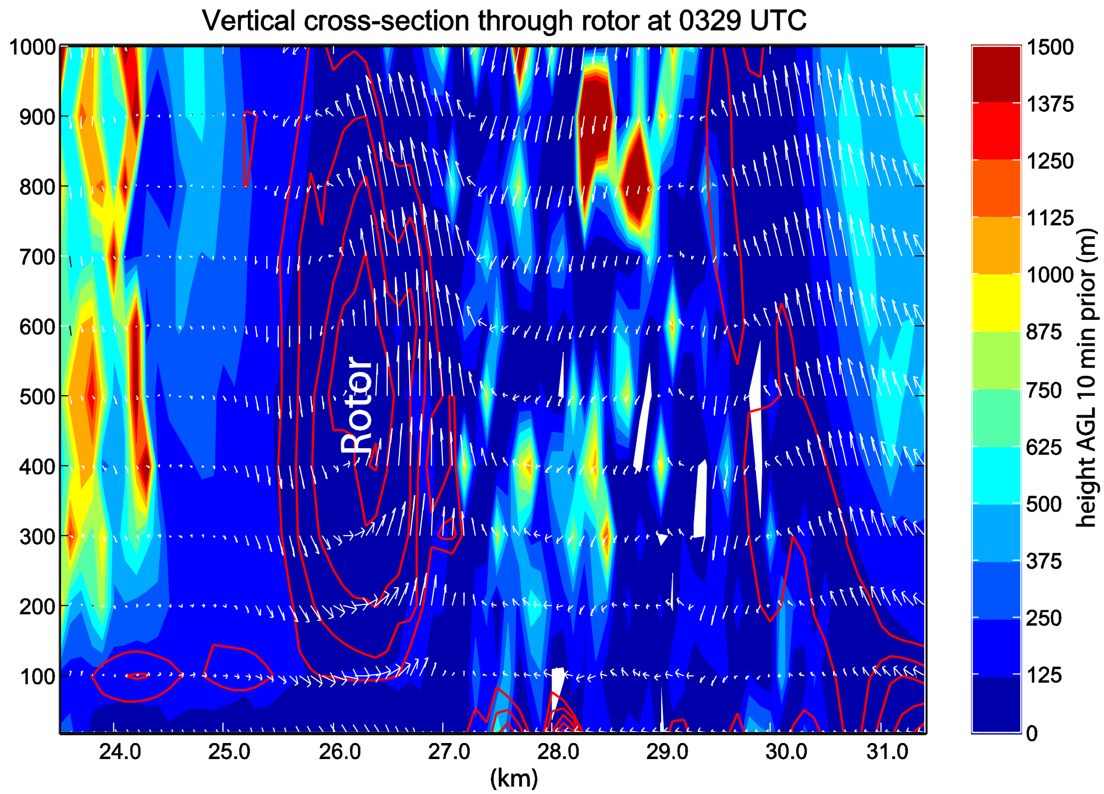

Fig. 11. Height AGL that a parcel in a present location at 0329 UTC was located at 0319 UTC (shaded, m AGL), together with the negative Y-component vorticity with a contour interval of 0.02 s^{-1} beginning at -0.04 s^{-1} (red contours), and the wind vectors in an east-west cross-section plane (m s^{-1}) along the black line in Fig. 8a.

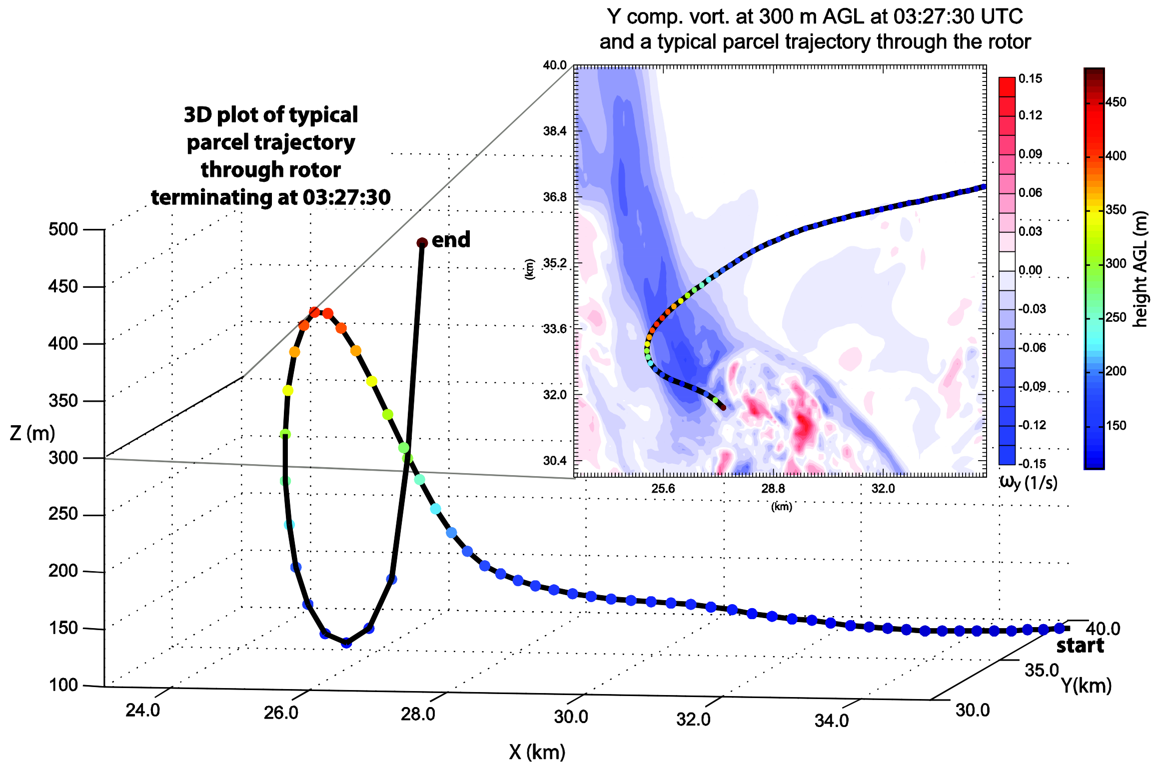

Fig. 12. Three dimensional plot (view from the south-southeast) of a typical parcel trajectory traveling through the rotor beginning at 0312:30 UTC and terminating in the rotor's upward branch at 0327:30 UTC. The inset is a XY cross-section plot of the y-component of horizontal vorticity (shaded, s^{-1}) at 0327:30 UTC overlaid with the two-dimensional projection of the trajectory. Dots along the trajectory are color coded by height AGL (m).

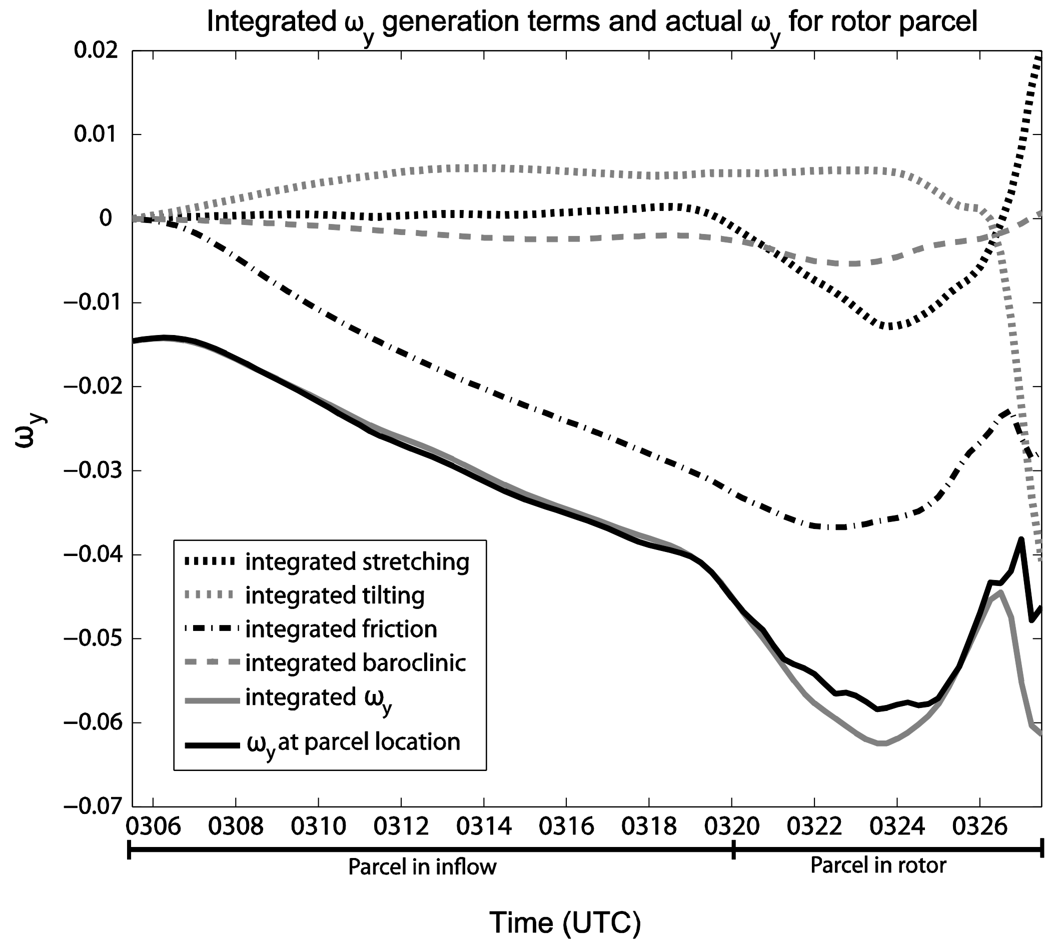

Fig. 13. Y-component vorticity budget for the parcel plotted in Fig. 12, but integrated backward in time until 0305:30 UTC. The parcel enters the rotor around 0320:00 UTC. The gray solid line is the sum of the time-integrated stretching (short dashed gray line), tilting (short dashed black line), frictional generation (alternating short-long black dashed line) and baroclinic generation (long dashed gray line). The solid black line represents y-component vorticity interpolated to the parcel location from the model grid at each time.

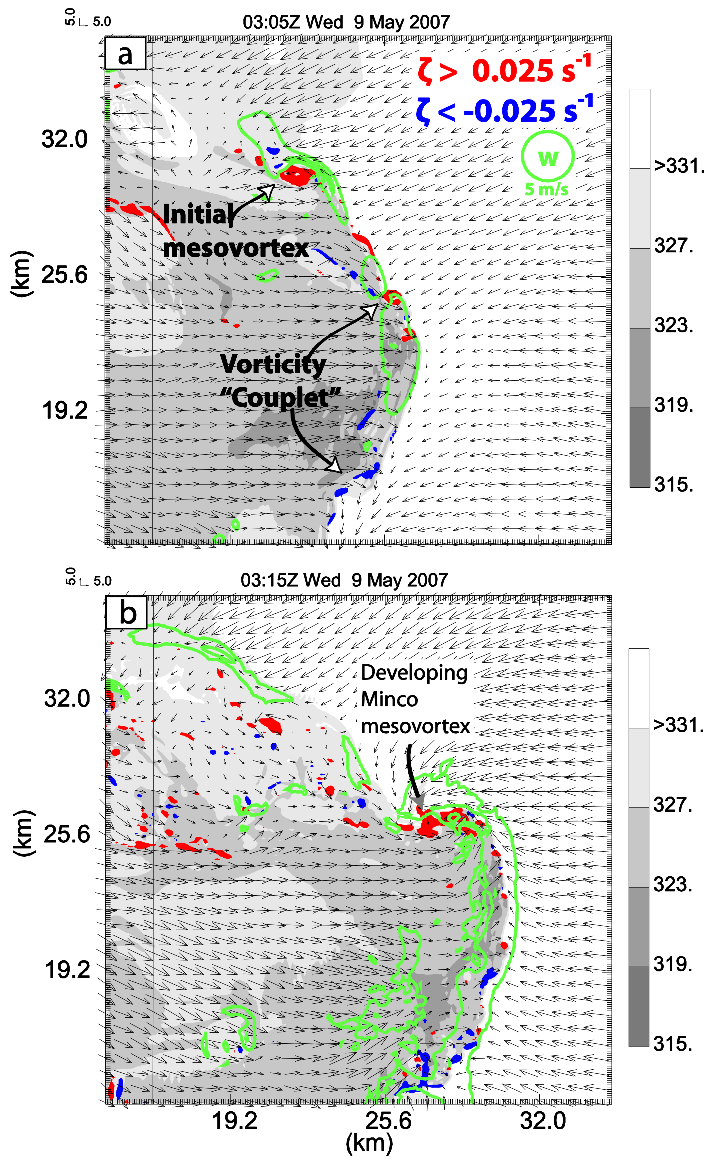

Fig. 14. As Fig. 2 but for the experiment with surface drag turned off and only at (a) 0305 UTC and (b) 0315 UTC.

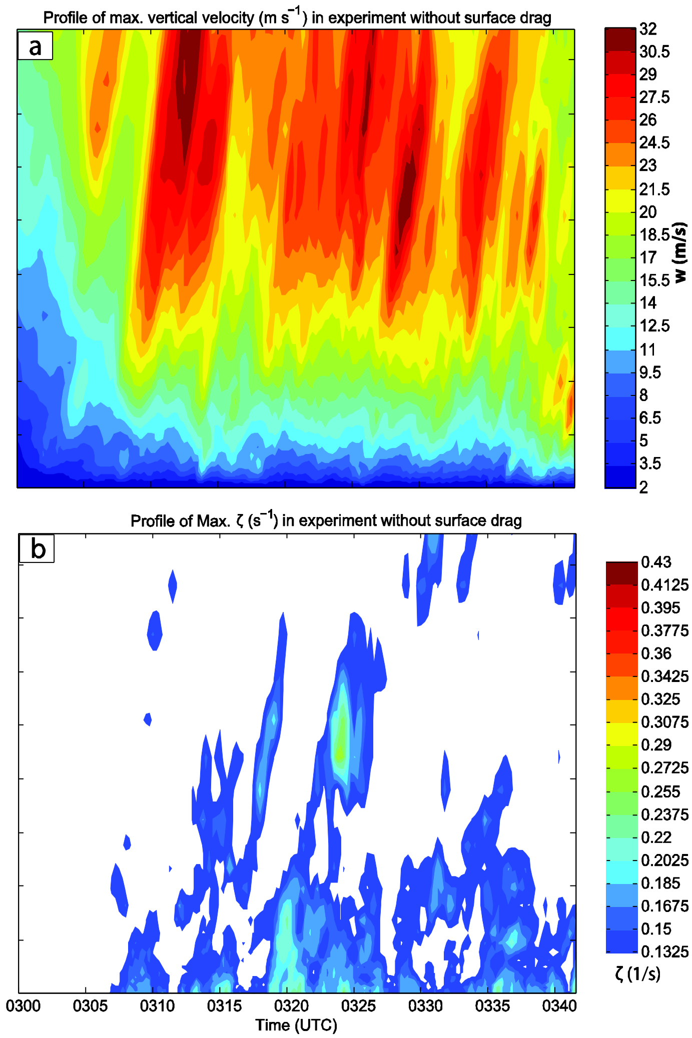

Fig. 15. As Fig. 6 but for the experiment with the surface drag parameterization turned off.

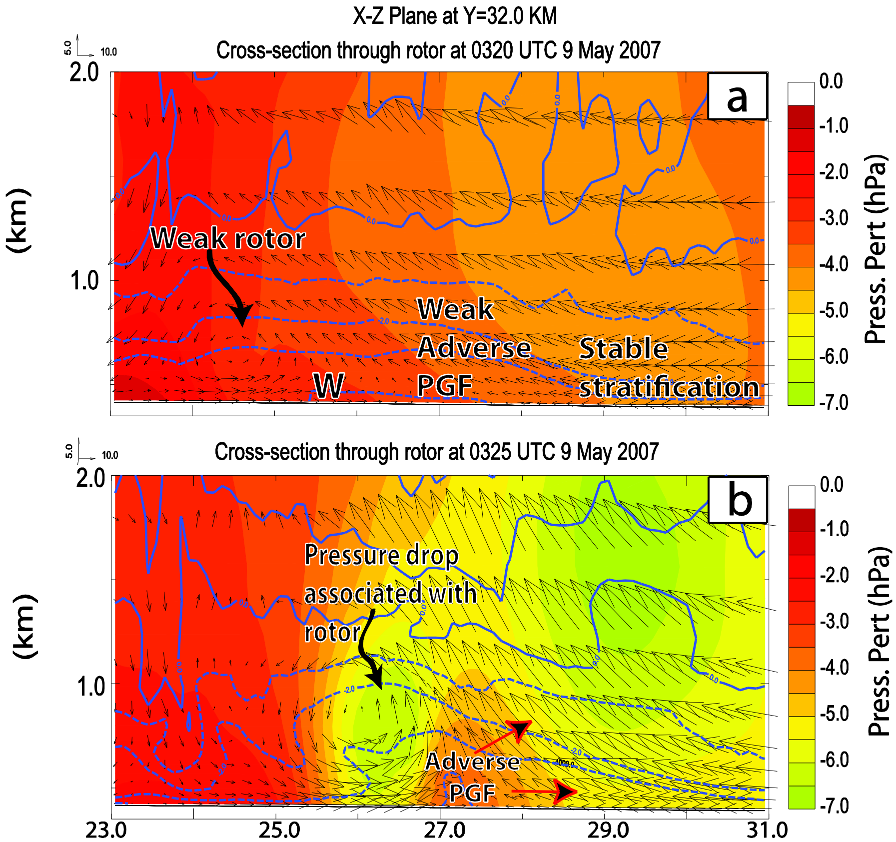

Fig. 16. Perturbation pressure (shaded, hPa), perturbation potential temperature (blue contours, K), and velocity in the plane of the cross-section (vectors, m s $^{-1}$) at (a) 0320 UTC and (b) 0325 UTC 9 May 2007. The 'W' in (a) marks the leading edge of the westerly momentum surge associated with the decaying initial mesovortex. The red-outlined arrows in (b) give the sense of the PGF direction.

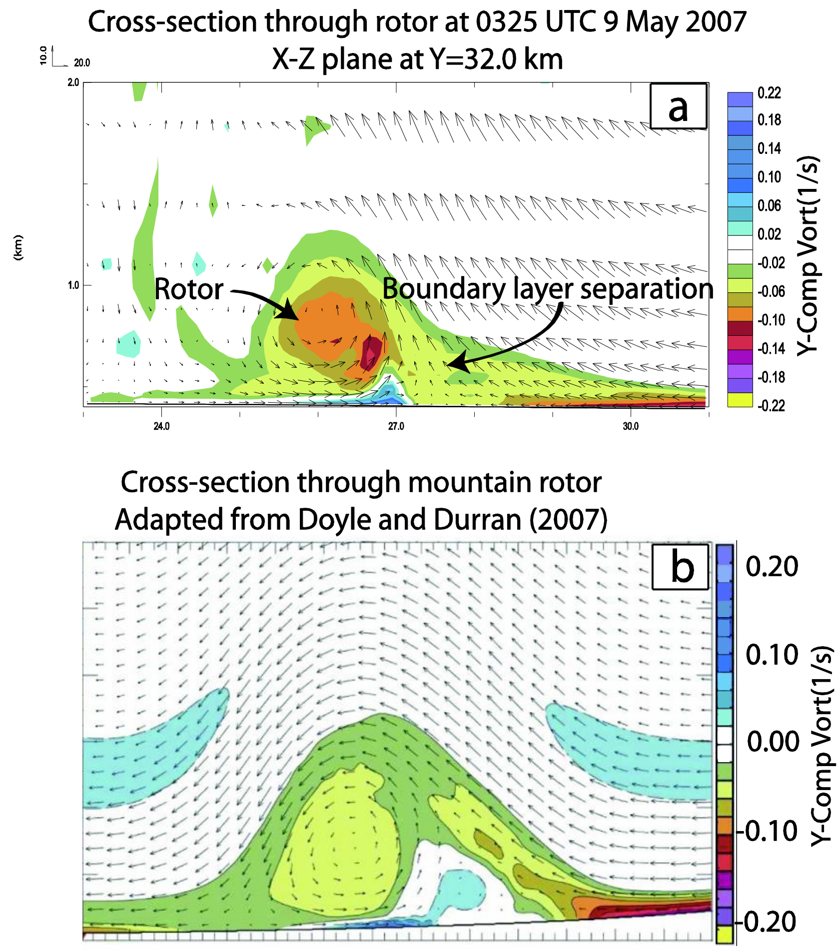

Fig. 17. Y-component vorticity (shaded, s^{-1}) and velocity vectors in the plane of the cross-section (vectors, m s^{-1}) from (a) an XZ crossection through the rotor at 0325 UTC and (b) from a XZ cross-section through a simulated rotor in the lee of a mountain [adapted from Doyle and Durran (2007)]. In (b), the original figure of Doyle and Durran (2007) has been reflected about the x-axis in order to directly compare with the flow geometry of the rotor in the 9 May 2007 case.

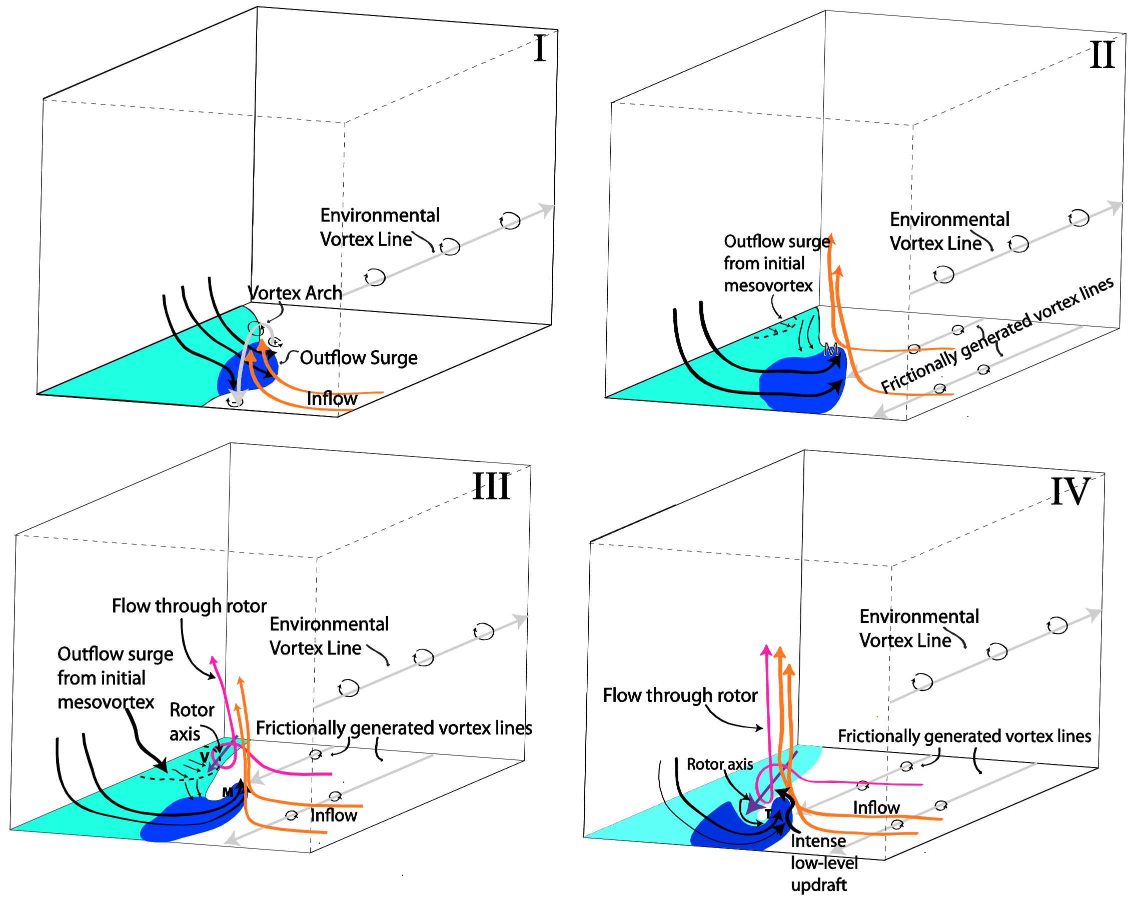

Fig. 18. Schematic of four-stage process leading up to TLV genesis. Vertical vorticity couplet development is depicted in (I). (II) shows the development of the dominant cyclonic Minco mesovortex and the associated development of frictionally-generated horizontal vorticity. (III) illustrates the development of the rotor. TLV genesis is shown in (IV). The cyan shading represents the cold pool. The dark blue shading represents the cold air within the cold pool bulge. Black arrows represent the surface flow trajectories. The orange arrows represent trajectories which enter the main updraft. The purple arrow in (III) and (IV) marks the horizontal rotor axis. The magenta arrows represent parcel trajectories that enter the rotor. Light gray vectors are idealized vortex lines. The 'M' represents the location of the Minco mesovortex. The dotted curves in (II) and (III) mark the location of the enhanced westerly momentum associated with the dissipation of the initial mesovortex. The 'v' behind the outflow surge from the initial mesovortex in (III) marks the location of the small area of vertical vorticity moving through the rotor. The 'T' in (IV) marks the location of the TLV.